JGR Solid Earth

RESEARCH ARTICLE
10.1029/2021JB022663

Rupture Heterogeneity and Directivity Effects in Back-Projection Analysis

Bo Li[1,2], Baoning Wu[2,3], Han Bao[4], David D. Oglesby[2], Abhijit Ghosh[2], Alice-Agnes Gabriel[1,5], Lingsen Meng[4], and Risheng Chu[6]

[1]Department of Earth and Environmental Sciences, Ludwig-Maximilians-University, Munich, Germany, [2]Department of Earth and Planetary Sciences, University of California, Riverside, CA, USA, [3]Department of Earth Sciences, University of Southern California, Los Angeles, CA, USA, [4]Department of Earth, Planetary and Space Sciences, University of California, Los Angeles, CA, USA, [5]Institute of Geophysics and Planetary Physics, Scripps Institution of Oceanography, University of California, La Jolla, CA, USA, [6]State Key Laboratory of Geodesy and Earth's Dynamics, Innovation Academy for Precision Measurement Science and Technology, Chinese Academy of Sciences, Wuhan, China

Key Points:

- We use kinematic forward models to investigate the relation between back-projection beam location, power and earthquake source properties
- Frequency-dependent back-projection peak beam power depends on the spatial heterogeneity near the rupture front, and rupture directivity
- We develop a novel framework to analyze frequency- and array-dependent back-projection results, including the 2019 M7.6 New Ireland Event

Supporting Information:

Supporting Information may be found in the online version of this article.

Correspondence to:

B. Li and B. Wu,
bli@gephyisik.uni-munechen.de;
bwu015@ucr.edu

Citation:

Li, B., Wu, B., Bao, H., Oglesby, D. D., Ghosh, A., Gabriel, A.-A., et al. (2022). Rupture heterogeneity and directivity effects in back-projection analysis. *Journal of Geophysical Research: Solid Earth*, *127*, e2021JB022663. https://doi.org/10.1029/2021JB022663

Received 22 JUN 2021
Accepted 12 FEB 2022

© 2022 The Authors.
This is an open access article under the terms of the Creative Commons Attribution-NonCommercial License, which permits use, distribution and reproduction in any medium, provided the original work is properly cited and is not used for commercial purposes.

Abstract

The back projection method is a tremendously powerful technique for investigating the time dependent earthquake source, but its physical interpretation is elusive. We investigate how earthquake rupture heterogeneity and directivity can affect back-projection results (imaged location and beam power) using synthetic earthquake models. Rather than attempting to model the dynamics of any specific real earthquake, we use idealized kinematic rupture models, with constant or varying rupture velocity, peak slip rate, and fault-local strike orientation along unilateral or bilateral rupturing faults, and perform back-projection with the resultant synthetic seismograms. Our experiments show back-projection can track only heterogeneous rupture processes; homogeneous rupture is not resolved in our synthetic experiments. The amplitude of beam power does not necessarily correlate with the amplitude of any specific rupture parameter (e.g., slip rate or rupture velocity) at the back-projected location. Rather, it depends on the spatial heterogeneity around the back-projected rupture front, and is affected by the rupture directivity. A shorter characteristic wavelength of the source heterogeneity or rupture directivity toward the array results in strong beam power in higher frequency. We derive an equation based on Doppler theory to relate the wavelength of heterogeneity with synthetic seismogram frequency. This theoretical relation can explain the frequency- and array-dependent back-projection results not only in our synthetic experiments but also to analyze the 2019 M7.6 bilaterally rupturing New Ireland earthquake. Our study provides a novel perspective to physically interpret back-projection results and to retrieve information about earthquake rupture characteristics.

Plain Language Summary

With the deployment of continental scale seismic arrays, seismologists can quickly locate the high-frequency seismic radiation sources and track the earthquake rupture propagation using a technique called back-projection. It is a signal beamforming technique application in seismology, and similar applications can be found in fields such as radar, wireless communication, and radio astronomy. Recent studies have proposed multiple advancements in improving the back-projection location. However, the physical interpretation of the amplitude of stacked high-frequency source radiations, which is commonly referred to as beam power, is still challenging since the analysis is not based on a forward model. In this article, we conduct a set of synthetic experiments to investigate the physical significance of back-projection beam power. We find that beam power is mainly controlled by the spatial heterogeneity wavelength near the rupture front, rupture directivity, and the seismogram frequency. It is in contrast with some previous studies that link the beam power to the maximum slip rate (acceleration) amplitude near the rupture front. Based on the results, we develop a novel theoretical framework that can quantitatively interpret the frequency- and array-dependent back-projection results not only in our synthetic experiments, but also the 2019 bilateral rupture M7.6 New Ireland earthquake.

1. Introduction

Signal beamforming is commonly used in sensor arrays for directional signal transmission or reception, with wide application in fields such as radar, wireless communication, and radio astronomy. In seismology, signal beamforming has been implemented since the deployment of seismic arrays back in the 1960s (Rost & Thomas, 2002). Its extensive application to resolve large earthquake source processes began in mid-2000 with the installation of continental scale seismic arrays, such as Hi-net (or Japan array) and US Array. One application of beamforming in

imaging earthquake rupture processes is commonly denoted as the back-projection method (Kiser & Ishii, 2017). Since its first successful application to study the rupture process of the 2004 Mw 9.2 Sumatra earthquake (Ishii et al., 2005; Krüger & Ohrnberger, 2005), the back-projection method has been widely applied to image ruptures of many large and moderate earthquakes (e.g., Bao et al., 2019; Fan & Shearer, 2015; Kiser & Ishii, 2011; Koper et al., 2011; Li & Ghosh, 2017; Meng et al., 2012; Tan et al., 2019; Xu et al., 2009; Yagi & Okuwaki, 2015; Yao et al., 2011; Yin et al., 2016; Zhang & Ge, 2010). Back-projection analysis tracks sources of high-frequency seismic radiation by shifting and stacking seismograms. It is different from traditional finite-fault inversion (e.g., Hartzell & Heaton, 1983) and dynamic rupture modeling (e.g., Mikumo & Miyatake, 1993), since it requires an estimation of the area that could potentially be ruptured in the event, but does not require prior constraints such as the fault geometry, initial stress, frictional strength conditions, and other source properties. In addition, back-projection doesn't need extensive computation to simulate the wavefield. Back-projection realization is thus relatively fast and the results are usually consistent among research groups if using the same data. In particular, the back-projection method is capable of utilizing seismic records up to a few Hz, which is usually computationally not feasible for traditional methods that aim to fit ground motion records via kinematic or dynamic earthquake source models (e.g., Gallovič et al., 2019; Liu et al., 2006). With all these benefits, back-projection has now become an important practice in earthquake science.

Multiple advancements have been proposed to improve the back-projection method in the past decade, such as the MUltiple SIgnal Classification (MUSIC, Meng et al., 2011), Compressive Sensing (Yao et al., 2011), hybrid back-projection (Yagi et al., 2012), Image Deconvolution back-projection (Wang et al., 2016), Phase-weighted stacking (Fan & Shearer, 2017), and Slow-Enhanced back-projection (Meng et al., 2018). Nevertheless, an essential issue has not been fully resolved: back-projection results are still ambiguous as to which physical processes on fault are being tracked. This ambiguity exists because the back-projection method does not provide an explicit physical expression for the underlying source process. Traditional inversion methods use a physical forward model such that output parameters have clear physical meanings (e.g., slip, rupture time, and moment). Conversely, the back-projection method tracks the source of high-frequency seismic radiation, which could derive from many different physical processes, such as a change of rupture velocity (including termination), heterogeneity of slip or slip rate, or variation of fault geometry (e.g., Madariaga, 1977; Madariaga et al., 2006; Spudich & Frazer, 1984). Spudich and Frazer (1984) specifically point out the difficulty to distinguish between the case of constant slip with variable rupture velocity and the case of constant rupture velocity with variable slip challenging all far-field waveform analyses. This ambiguity complicates the interpretation of back-projection results. Thus, more theoretical efforts are needed to help us make better use of this technique.

In this study, we use one-dimensional kinematic rupture models and only allow one rupture parameter (rupture velocity, peak slip rate, and fault-local strike orientation) to vary in each model, to investigate the direct relation between different rupture parameters and back-projection results. We do not attempt to model rupture dynamics of any real earthquake, where different rupture parameters, such as the stress drop, rupture velocity, slip rate and slip direction (rake), can correlate (e.g., Schmedes et al., 2010). Previous studies suggest that under certain assumptions, the amplitude of back-projection beam power can correlate with the amplitude of slip or slip rate at the back-projected fault location (Fukahata et al., 2014; Okuwaki et al., 2019; Yao et al., 2012; Yin & Denolle, 2019). In contrast, our synthetic experiments show the back-projection beam power is affected by heterogeneity near the rupture front, and modulated by the rupture directivity. Based on Doppler theory that accounts for rupture directivity, we build a quantitative relation between heterogeneity wavelength and seismogram frequency. We use this relation to interpret the back-projection results of the 2019 M7.6 New Ireland earthquake. Our results, while highlighting limitations of the back-projection method, provide a novel theoretical framework to extract useful information about rupture processes from back-projection analyses of natural complex earthquakes.

2. Model Setup

The general workflow of our method is illustrated in Figure 1a. First, we design a set of kinematic source models, in which we set the rupture process parameters. Next, we compute the corresponding synthetic seismograms at a teleseismic array. Finally, we perform the back-projection analysis using these synthetic seismograms, filtered in multiple frequency ranges, and compare back-projection results with the pre-determined rupture models. The

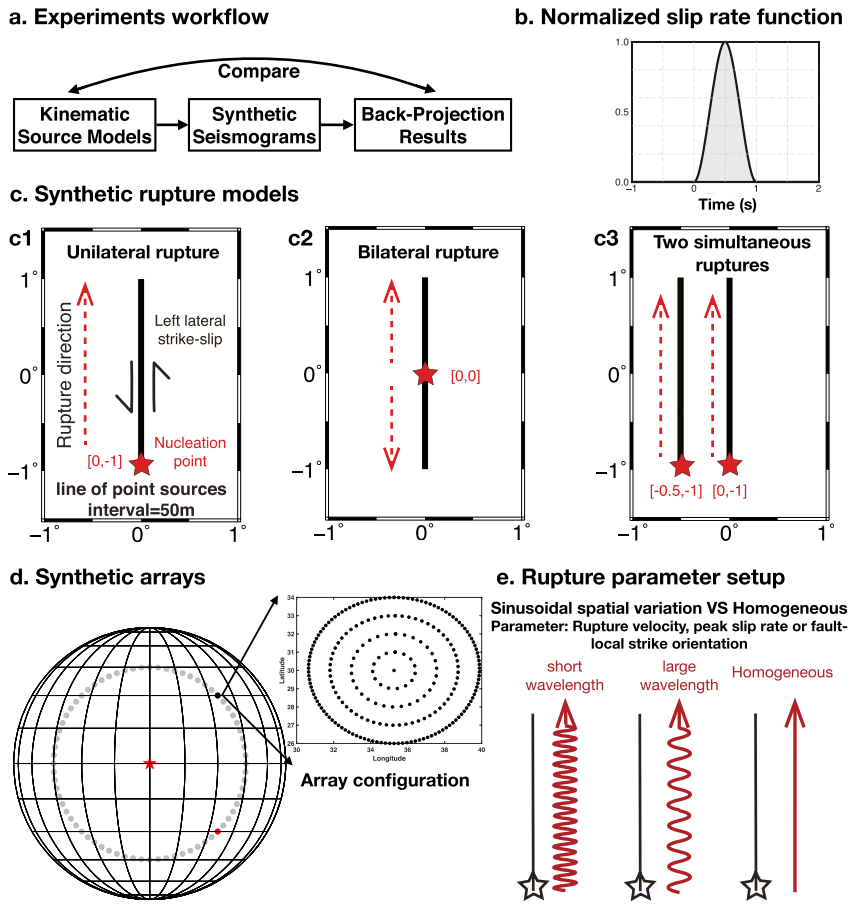

Figure 1. Diagrams showing the workflow and setup of our synthetic experiments. (a) General workflow of our experiments. (b) The normalized cosine slip rate function of the propagating slip pulse used in all our experiments. (c) 1D fault geometries and rupture directivity used throughout. (d) Teleseismic arrays setup at a distance of 45° from the source region. Each circle in the global scale map represents one array in a different azimuthal direction. The arrays have the same configuration and each consists of 230 stations, shown in the inset. Results for the array at 45 azimuthal degrees (black circle) are discussed in detail. Results for the array at 135 azimuthal degrees (red circle) are shown in Figure S3 in Supporting Information S1. Red star: fault location. (e) Schematic of rupture propagation with different variation wavelengths of model parameters along the fault. Except for a reference homogeneous model, all ruptures in our experiments have one property (slip rate, local rupture velocity, local strike orientation) that varies sinusoidally in space. We test a wide range of variations in wavelength and amplitude of the three parameters while keeping other parameters constant.

kinematic models are specifically designed such that they isolate the effects of different source processes on the back-projection result.

2.1. Source Models

The source models are quite simple to isolate the effects of individual physical parameters. As Figure 1c shows, we simulate hypothetical earthquakes occurring at the equator at the prime meridian (latitude-0°, longitude-0°; note that the absolute positions of the source and receiver array are not relevant). We model 1D left-lateral events rupturing either a single or two parallel north-south striking faults. All models use a line of double-couple moment tensor point sources with intervals of 50 m. We use a small enough spacing between point sources to avoid introducing artificial high-frequency signals in the back-projection results (see Section 5.5.4). To model both simple and complex fault ruptures, and investigate the effects of rupture directivity, we design three types of rupture models: a unilateral rupture that propagates from the south to north on a single fault (Figure 1c1), a bilateral rupture that nucleates at the center of a fault (Figure 1c2), and two simultaneous unilateral ruptures that propagate from the south to north on two parallel faults (Figure 1c3). We also investigate north-to-south unilateral

rupture models, which generate the same results as moving the array location to the equatorially symmetry location. The model with two simultaneous rupture branches is a simplified analog for a complex rupture, in which multiple rupture fronts with different properties propagate simultaneously at different spatial locations. All models have an average rupture velocity of 3 km/s.

In our kinematic models, rupture propagation is modeled as a propagating slip pulse (e.g., Haskell, 1964). The slip rate function (Figure 1b) is defined as:

$$\dot{D}(t) = 0.5 \times \left(-\cos\left(\frac{2\pi t}{T}\right) + 1\right) \times \dot{D}_{peak}, \quad t \in [0, T]. \tag{1}$$

$\dot{D}(t)$ is the slip rate at time t. $T = 1$ s is the constant rise time (Figure 1b) for all sources. $\dot{D}_{peak}$ is the peak slip rate. We spatially vary three rupture properties: (a) local pulse propagation velocity (rupture velocity), (b) peak slip rate, and (c) fault-local strike orientation/radiation pattern of the linear point sources. The rupture properties are set to either spatially vary in a sinusoidal manner or be homogeneous in all experiments, as shown in Figure 1e. The wavelength and amplitude of the sinusoidal variations are adjustable parameters in our experiments. We assume purely sinusoidal variation because it is the basis of Fourier transform, and thus renders the analysis of the back-projection results with respect to the wavelength of the variability straightforward; more realistic ruptures would of course be represented by the sum of many different wavelength components. We will elaborate on the choice of purely sinusoidal variations in Section 5.4.2.

2.2. Computing Synthetic Far-Field Seismograms

To investigate the direct effect of source radiation on back-projection results, we consider a homogeneous spherical Earth with P wave velocity $V_p = 5.6$ km/s, density $\rho = 2{,}750$ kg/m^3 and shear modulus $\mu = 3 \times 10^{10}$ Pa, and use a full space Green's function (i.e., the Green's function from a homogeneous, unbounded medium) to compute synthetic far-field P waves with the analytical solution given in Aki and Richards (2002):

$$\boldsymbol{u}(\boldsymbol{x}, t) = \frac{1}{4\pi\rho {V_p}^3} \boldsymbol{A}^{FP} \frac{1}{r} \dot{M}_0 \left(t - \frac{r}{V_p}\right), \tag{2}$$

where u is the far-field P wave displacement vector, x is the receiver location, A^{FP} is the radiation pattern factor of the far-field P wave described in Equation (4.33) in Aki and Richards (2002), r is the distance between the source and receiver, and $\dot{M}_0$ is the moment rate function.

Figure 1d illustrates a range of teleseismic arrays at a distance of 45° away from the source region. All arrays are at 0 km depth and have the same configuration, which is with an aperture of 8°, and consists of 230 stations arranged in five concentric circles. To better quantify the rupture directivity effect, we do not set the array aperture to resemble continental-scale (e.g., North American or European) arrays. We use a circular array and our synthetic results show back-projection is able to successfully image the rupture propagation on the fault, indicating the array configuration will not affect our back-projection analysis. We focus on a synthetic teleseismic array centered at 30° N, 35.2644° E, which is 45° northeast azimuth and 45° epicentral distance away from the fault center [0°, 0°] for detailed analysis (Figure 1d). To investigate the effect of array azimuth, we also use arrays with the same configuration, but varying the azimuth of the array center from 0 to 355° relative to the fault center, with 5° interval (gray circles in Figure 1d).

Synthetic seismograms are of 1,500 s duration, with a sampling rate of 20 Hz. We calculate the direct P wave for the vertical components at the array, which is generally used in back-projection analysis. This method helps eliminate signal contamination from other body or surface phases, and links our results directly to the rupture front. The relatively small aperture results in coherent synthetic seismograms across the array, even for arrays across the nodal planes (Figure S1 in Supporting Information S1). We note the array azimuth does not affect our analysis of the source heterogeneity and rupture directivity effects on back-projection results in the synthetic experiments. Back-projection results using arrays across the nodal plane and an array located to the southeast of the source region are shown in Figures S2 and S3 in Supporting Information S1, respectively.

Our kinematic source models are Haskell-type models (Haskell, 1964), where the rupture propagation initiates and terminates rather abruptly, which produces high amplitude seismic radiation (e.g., Madariaga, 1978) from starting and stopping phases. We separate the rupture propagation radiation from the starting/stopping phase radiation by utilizing a fault long enough to ensure that both types of radiation are separated in time in the seismograms.

2.3. Back-Projection Method

The back-projection method uses the curvature of the wavefront recorded at large-aperture, dense seismic arrays, and the time reversal property of these coherent waves, to determine the time and location of their sources (Ishii et al., 2005). In our synthetic tests we use a classic linear back-projection method from Ishii et al. (2005) and Kiser and Ishii (2017). For the 2019 M7.6 New Ireland earthquake, we employ both the linear back-projection (Section 4.3) and the advanced Multitaper-MUSIC back-projection (Figure S4 in Supporting Information S1) method (e.g., Bao et al., 2019; Meng et al., 2011) to verify that our analysis and interpretation do not depend on a particular implementation of back-projection.

For our linear back-projection, we define the source region in the synthetic experiments as a box from 1.5°S to 1.5°N and from 1.0°W to 1.0°E (Figure 1c), although we note that the absolute position of our source-receiver combination is not significant. We divide this box into grids with 0.05° spacing in latitude and longitude. The travel times from the source grids to each station are calculated using our homogeneous velocity model (5.6 km/s for the P wave), which rules out travel time errors due to the wave propagation from source grids to array stations. Thus, no time calibration is required.

The relative radiation energy of each source region grid is then calculated by stacking the waveforms of all stations after correcting for moveout. The linear stack across the array can be expressed as (Kiser & Ishii, 2017):

$$s^j(t) = \sum_{i=1}^{N} w^{ij} u_i \left(t + \tau^{ij}\right), \tag{3}$$

where $s^j(t)$ is the stacked time series of N stations, corresponding to source grid point j. $u_i(t)$ is the observed displacement, velocity, or acceleration time series at station i; we use the velocity seismogram. τ^{ij} is the travel time from source j to station i, and w^{ij} is a weighting factor that is used to adjust the polarity and normalize $u_i(t)$. The beam power or beam energy at time t is computed as an integral of $s_j^2(t)$ over a sliding time window from t to $t + t_w$. The chosen length of the sliding window is an important factor that may affect the stability and accuracy of the analysis, and balances trade-offs between resolution and other arrivals and noise. Generally, the beam power should be proportional to the absolute level of $s_j^2(t)$, which depends on the number of stations. However, the relative beam power between radiation sources is thought to represent the relative radiation strength of these different sources. If beam power is significantly high relative to its background value in the defined study region, we may infer that grid point j contains a significant radiation source at time t. We use the grid location with the maximum beam energy in a given time window to represent the source location determined by the back-projection in that time window.

As Equation 3 suggests, the back-projection method tracks sources that generate high or dominant amplitude signals in the filtered frequency ranges across the array. However, it cannot distinguish which type or types of many possible physical processes are producing the high amplitude signals. However, in our forward modeling experiments, we can interpret the back-projection result by comparing it with the corresponding pre-determined source model, and hence determine the effects of different source processes.

3. Back-Projection Analysis With Synthetic Rupture Models

We present back-projection results for several synthetic rupture models. We start with the simplest rupture model where all the three variable rupture parameters (local rupture velocity, peak slip rate and fault-local strike orientation) are spatially homogeneous on the fault. Next, we allow these rupture parameters to vary along the fault to investigate how heterogeneity in kinematic parameters influences back-projection results. We then set simultaneous ruptures on two parallel faults with different heterogeneity wavelengths to further demonstrate the

heterogeneity effect. Lastly, we conduct bilateral rupture experiments to investigate the effect of rupture directivity. A summary of our synthetic models and rupture parameters can be found in supplementary Tables S1 and S2 in Supporting Information S1.

3.1. Back-Projection Analysis for the Unilateral & Homogeneous Rupture on a Single Fault (Model A1)

Large earthquake ruptures in the real world are often very complex (e.g., Hamling et al., 2017; Hayes et al., 2010; Ross et al., 2019; Sieh et al., 1993; Toksoz et al., 1999). We first consider a simple source model with a unilateral, homogeneous rupture on a north-south striking fault. This model is referred to as Model A1. The rupture nucleates at the southern end of the fault [0° 1° S], and propagates to the north. All rupture parameters are uniform along the fault. An overview of the model settings can be found in Table S1 in Supporting Information S1 and Figures 2a1 and 2b1.

The back-projection results using the synthetic seismograms filtered between 1 and 2 Hz are shown in Figure 2c1. Colored circles show the rupture source location determined by the back-projection in a 6-s sliding time window, with a 1-s time step. Circle size is proportional to maximum beam power, which indicates the relative amount of seismic energy radiation from the rupture sources in the corresponding time window. Only the starting and stopping points of rupture have strong beam power and are located by the back-projection method. There is negligible beam power (circles are too small to be visible) as the rupture propagates over the bulk of the fault, so back-projection fails to track the rupture propagation (Figure S5 in Supporting Information S1). This effect is also illustrated in the integrated beam power for the whole rupture duration (Figure 2d1). Due to its simplicity, such an extreme outcome is highly improbable for a real-world earthquake. Nevertheless, this simple homogeneous model A1 can serve as a reference model when analyzing more heterogeneous models.

We note the northeast-southwest direction elongated lobes in the summed energy (Figure 2d1). This artifact persists in the back-projection result of each time window and is due to the array response function (ARF; Figure S6). The ARF is constrained by the array configuration, distance and azimuth relative to the rupture sources (Xu et al., 2009), and also reflects the spatial resolution of the back-projection analysis. Evaluating the spatial resolution of back-projection results is important for a real earthquake. However, we use the same teleseismic array and source region throughout, so the ARF in all experiments are identical, and our analysis of the synthetic experiments will not be affected by ARF-related effects.

3.2. Back-Projection Analysis for the Unilateral & Heterogeneous Rupture on a Single Fault (Model A2, A3, and A4)

Next we investigate the capability of back-projection to image heterogeneous rupture processes. We set up three models (Models A2, A3, and A4); in each of them we allow one rupture parameter (rupture velocity, peak slip rate or fault-local strike orientation) to vary spatially via a harmonic (sinusoidal) function, with a constant variation amplitude and spatial wavelength along the fault. Such a highly idealized setup allows a straightforward analysis of the effects of heterogeneity (see also Section 5.4.2). A summary of the rupture parameters is in Table S1, and an overview of the forms of spatial heterogeneity is shown in Figures 2a2–2a4 and b2–b4.

The back-projection maximum beam energy trajectory and the time-integrated beam energy of Models A2, A3, and A4 are shown in Figures 2c2–2c4 and d2–d4, respectively. We use the same array and 1–2 Hz filter as in Model A1. Back-projection successfully tracks the rupture process for all three heterogeneous models, although model A4 (variable fault-local strike) produces slightly less accurate locations, with the apparent source displaced slightly from the true source. In addition to the large energy radiation at the starting and stopping rupture stages observed in homogeneous Model A1, energy of comparable amplitude is released throughout the rupture in all heterogeneous models, with all heterogeneous models having a similar character. Differences in beam power between the different models could be equalized by simply modifying the amplitude and wavelength of the variation. Therefore, back-projection can locate the high frequency radiation sources during heterogeneous rupture process, but is unable to distinguish the physical processes responsible for the seismic radiation.

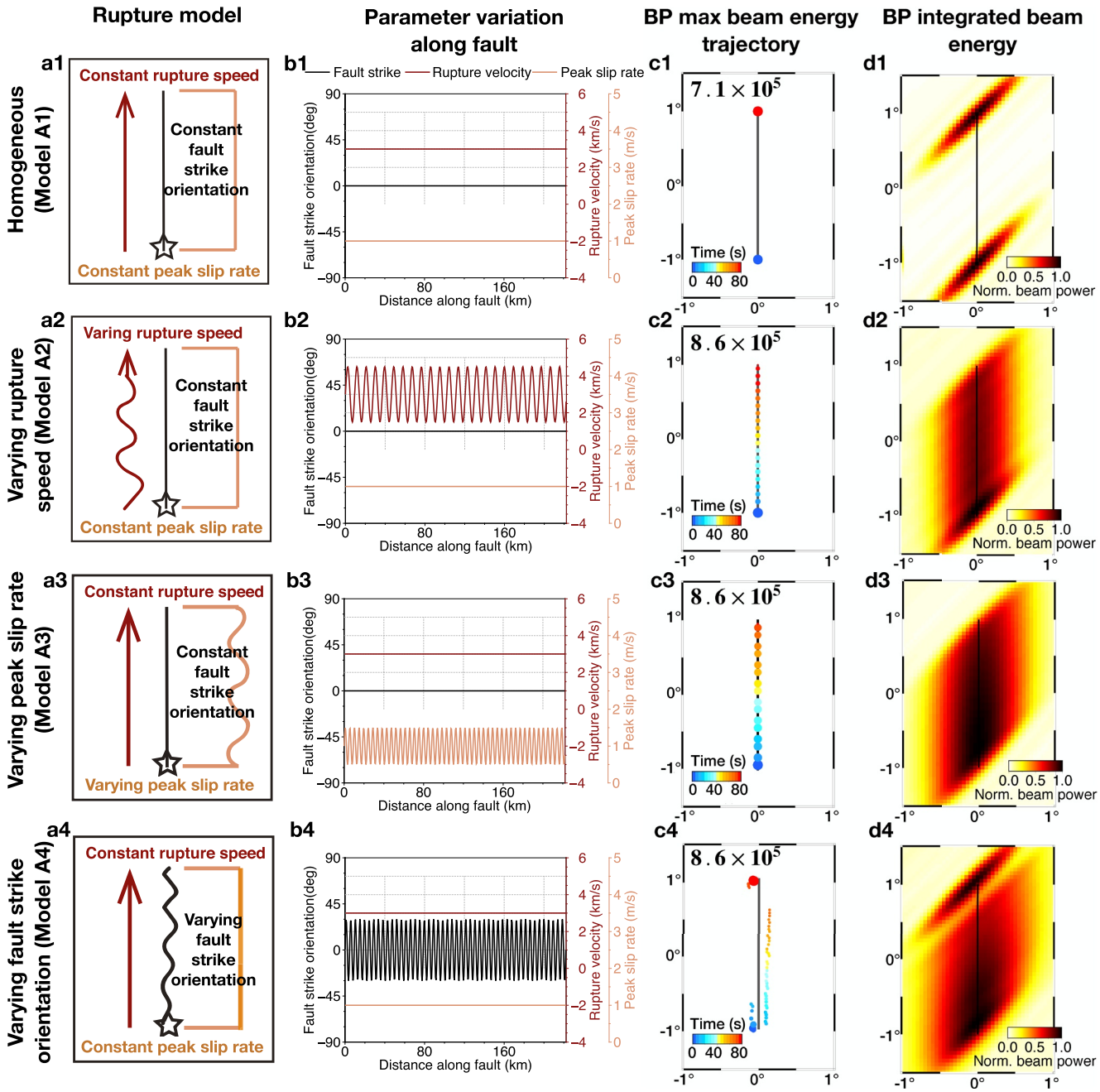

Figure 2. Unilateral rupture models (Model A) and back-projection results. (a) Schematics of 4 kinematic source models with rupture propagating unilaterally from the south to north. a1–a4 correspond to the homogeneous, variable rupture velocity, variable peak slip rate, and variable fault-local strike orientation models, respectively. (b) Parameter settings along the fault in each model described in (a). (c) Rupture process imaged by back-projection for each model described in (a), using 1–2 Hz filtered synthetic seismograms. Color coded circles represent the grid location with the highest beam energy in each 6-s back-projection sliding time window (blue-early, red-late), with the size proportional to the maximum beam power (numbers in c1–c4) in each experiment. (d) The integrated beam power (normalized through the full back-projection imaging domain and time series) for the complete rupture duration for the corresponding models described in (a).

3.3. Frequency and Heterogeneity Wavelength Dependent Results for Unilateral & Heterogeneous Rupture on a Single Fault (Model A5)

While it may not be possible to infer which type(s) of fault heterogeneity are responsible for the beam power at any given time, it is possible to extract spatial wavelength information about the heterogeneity from back-projection results by performing back-projection analyses with seismograms filtered in different frequency bands.

Previous studies have suggested that a back-projection result with lower/higher frequency seismograms reveals the part of rupture process that has a larger/smaller asperity size (e.g., Kiser & Ishii, 2011; Lay et al., 2012; Yao et al., 2013), which is analogous to the longer/shorter heterogeneity wavelength in our synthetic experiments. This conceptually plausible idea has not been quantitatively tested to the best of the authors' knowledge.

To explore the effect of rupture heterogeneity on frequency-dependent back-projection results, we set up a total of 66 kinematic models based on Model A2 (sinusoidally variable rupture velocity). Peak slip rate (1 m/s) and fault-local strike orientation (0°) are invariant in all models. We refer to these models as Model A5 (see Table S1 in Supporting Information S1). As noted above, models with variable slip rate and strike produce comparable results, so we focus on rupture velocity for this analysis. V_{rup} is defined as a sinusoidal function with two variable parameters, the normalized variation amplitude (α) and the variation wavelength (λ).

$$V_{rup}(x) = V_0 + \alpha V_0 sin\left(\frac{2\pi x}{\lambda}\right). \tag{4}$$

Average rupture velocity V_0 is 3 km/s in our models. Note that $\alpha = 0$ indicates that there is no change in the rupture velocity, reducing to the homogeneous rupture model A1. Correspondingly, $\alpha = 0.5$ means that the rupture velocity varies between 1.5 and 4.5 km/s. As shown in Table S1 in Supporting Information S1, we construct kinematic models with different combinations of α (0, 0.1, 0.2, 0.3, 0.4 and 0.5) and λ (1.6, 2.0, 2.3, 2.8, 3.7, 4.6, 9.2, 18.3, 27.5, 55 and 220 km). We perform the back-projection analysis on each of these models with seismograms filtered in three different frequency bands: 0.1–0.5, 1–2, and 3–5 Hz, corresponding to $66 \times 3 = 198$ back-projection results.

As shown in the back-projection results of models A1–A4 (Figure 2), the starting and stopping stage of rupture generate significant radiation clearly resolved in the back-projection results. With no noise and no contamination from other seismic phases nor P-coda interferences, the synthetic P wave back-projection can image the rupture process in a wide parameter (α and λ) range. To quantitatively compare the energy radiation efficiency among models, we define the self-normalized rupture beam power P_i^{SN} during the rupture propagation for a given synthetic back-projection experiment as:

$$P_i^{SN} = \tilde{P}_i(t)/\max\left(P_i(t)\right). \tag{5}$$

For each experiment i, we first find the largest beam power amplitude P_i among all source grids for a given time-window $[t, t + t_w]$, and do this for all sliding time windows during the rupture process to obtain the "maximum beam power" time series $P_i(t)$ for the experiment. Next, we use the ratio between the median $\tilde{P}_i(t)$ and maximum $\max(P_i(t))$ of the $P_i(t)$ to calculate the self-normalized rupture beam power $P_i^{SN}$for the experiment. $\tilde{P}_i(t)$ always represents the energy radiation during the rupture propagation process, while $\max(P_i(t))$ always corresponds to the starting/stopping phase. P_i^{SN} close to 0 indicates insignificant energy radiation during the rupture propagation (relative to the starting/stopping phase), resulting in the rupture process being non-trackable (e.g., Figures 2c1 and S5 in Supporting Information S1). P_i^{SN} approaching 1 (e.g., Figures 2c2–2c4) indicates significant energy radiation during the rupture propagation, and the rupture process is more likely to be imaged.

Figure 3a shows an overview of P_i^{SN} of all the 198 synthetic experiments. The left (a1), middle (a2), and right (a3) panels illustrate the results of each of the 66 experiments using synthetic seismograms filtered in 0.1–0.5, 1–2 and 3–5 Hz, respectively. Each color-coded dot in these plots represents P_i^{SN} in one experiment. The P_i^{SN} of all experiments varies between 10^{-9} and 1.

Our synthetic experiments show that in all three frequency bands, the case of $\alpha = 0$ (homogeneous rupture, Model A1) results in low P_i^{SN}, such that the rupture process cannot be properly imaged by back-projection. Only heterogeneous ruptures can produce high P_i^{SN}, in a limited range of λ in each frequency band. Our results show that within a single frequency band, the wavelength range of efficient rupture energy radiation ($P_i^{SN} > 0.01$; blue-shaded area in Figure 3a) becomes wider when α increases from 0.1 to 0.5. We also notice that when filtering in a higher frequency band, from 0.1–0.5 Hz to 1–2 Hz then to 3–5 Hz, the efficient energy radiation corresponds to shorter heterogeneity wavelengths. This result quantitatively supports the popular idea that back-projection analysis in low/high frequencies tends to image large/small size fault heterogeneities, or fault asperities (e.g., Yao et al., 2013).

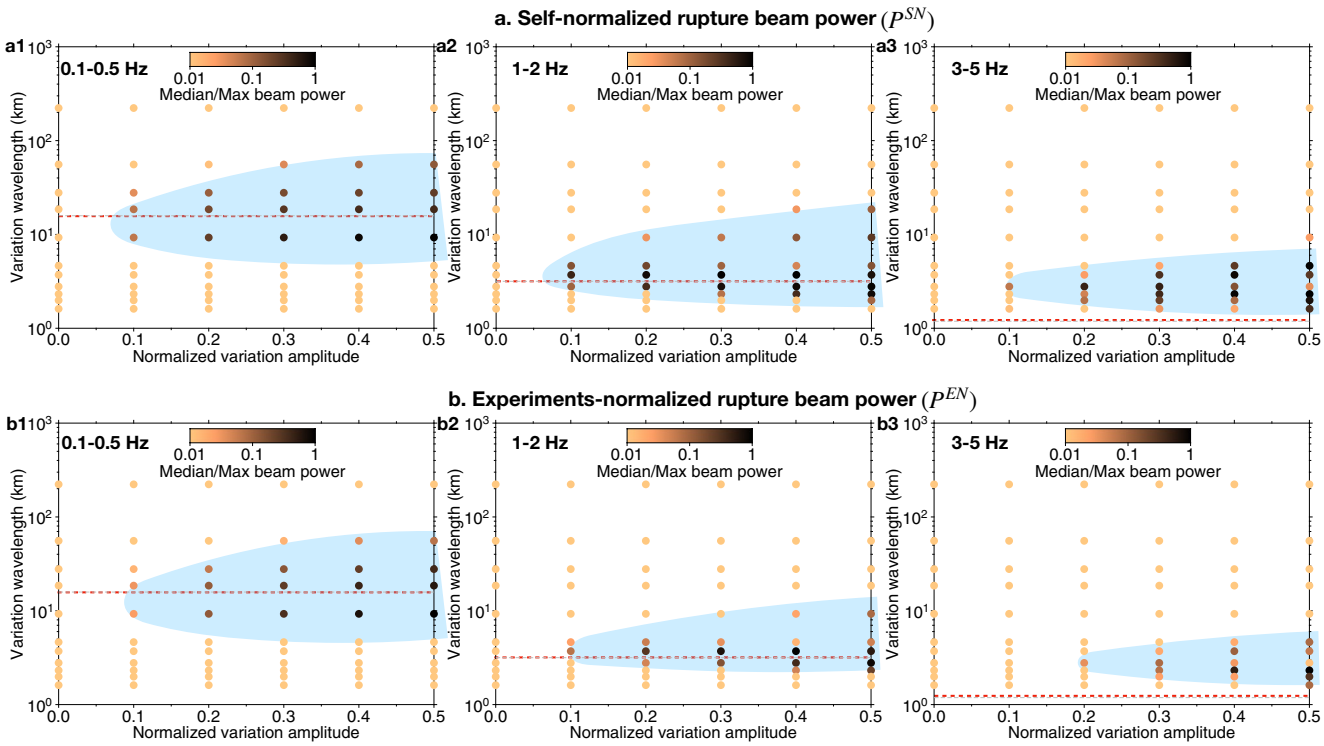

Figure 3. Phase diagrams of the normalized rupture beam power (defined in Equations 5 and 6). (a) Overview of self-normalized rupture beam power (Equation 5) results. Left, middle, and right panels show 66 experiments in frequency range 0.1–0.5, 1–2, and 3–5 Hz, respectively. Each color-coded (in a logarithm scale) dot in the figure represents one experiment, with x-coordinate denoting the relative fluctuation amplitude α and y-coordinate denoting the heterogeneity wavelength λ. The dark color indicates higher amplitudes in the array spectrum in the filtered frequency ranges, and the rupture sources would be more likely to be captured by the back-projection using the array data. The blue-shaded area marks the parameter space where the normalized beam power has values above 0.01, which we use as a threshold to consider the energy radiation efficiency. The horizontal red dashed lines denote the corresponding heterogeneity wavelength for the central frequency (0.3, 1.5 and 4 Hz) of the three filtered frequency bands according to Equation 8. (b) Same as (a), but for the experiment-normalized rupture beam power (see Equation 6).

In Equation 3, the seismograms are first normalized by the weighting factor w^{ij} before stacking. In our experiments so far, we normalize each seismogram to the peak amplitude of its own time series, which corresponds to the strong starting/stopping phase. Due to the variation of the parameters α and λ, the amplitudes of the starting/stopping phase could be different. In order to directly compare the absolute energy radiation during the rupture propagation among models in A5, we also perform the back-projection analysis without the weighting factor $w^{ij}$and define the experiment-normalized rupture beam power P_i^{EN} as below:

$$P_i^{EN} = \tilde{P}_i(t)/\max\left(\tilde{P}_1(t), \tilde{P}_2(t), \ \ldots, \tilde{P}_{66}(t)\right). \tag{6}$$

For this analysis, we first find for each of the 66 experiments the $\tilde{P}_i(t)$ that represents the median energy radiation during the rupture process for that experiment. We then normalize $\tilde{P}_i(t)$ to the maximum median value $\max\left(\tilde{P}_1(t), \tilde{P}_2(t), \ \ldots, \tilde{P}_{66}(t)\right)$ across all 66 experiments to calculate the experiment-normalized rupture beam power P_i^{EN}.

Since the normalizing factor $\max\left(\tilde{P}_1(t), \tilde{P}_2(t), \ \ldots, \tilde{P}_{66}(t)\right)$ is the same for all 66 experiments, we can use P_i^{EN} to directly compare the rupture beam power across different experiments and exclude the effects of strong starting/stopping phases. As shown in Figure 3b, although the details differ slightly from the self-normalization analysis, we qualitatively observe the same frequency-dependent pattern as in P_i^{SN} (Figure 3a), in which a shorter heterogeneity wavelength results in more high frequency energy radiation. Also, we find that the absolute amplitude of P_i^{EN} for the "un-imaged" experiments (none-shaded phase) is several orders of magnitude smaller than that in the "imaged" experiments (blue-shaded phase). These results imply that our analyses of P_i^{SN} are not affected by the likely unrealistically sudden rupture initiation and termination in the synthetic models.

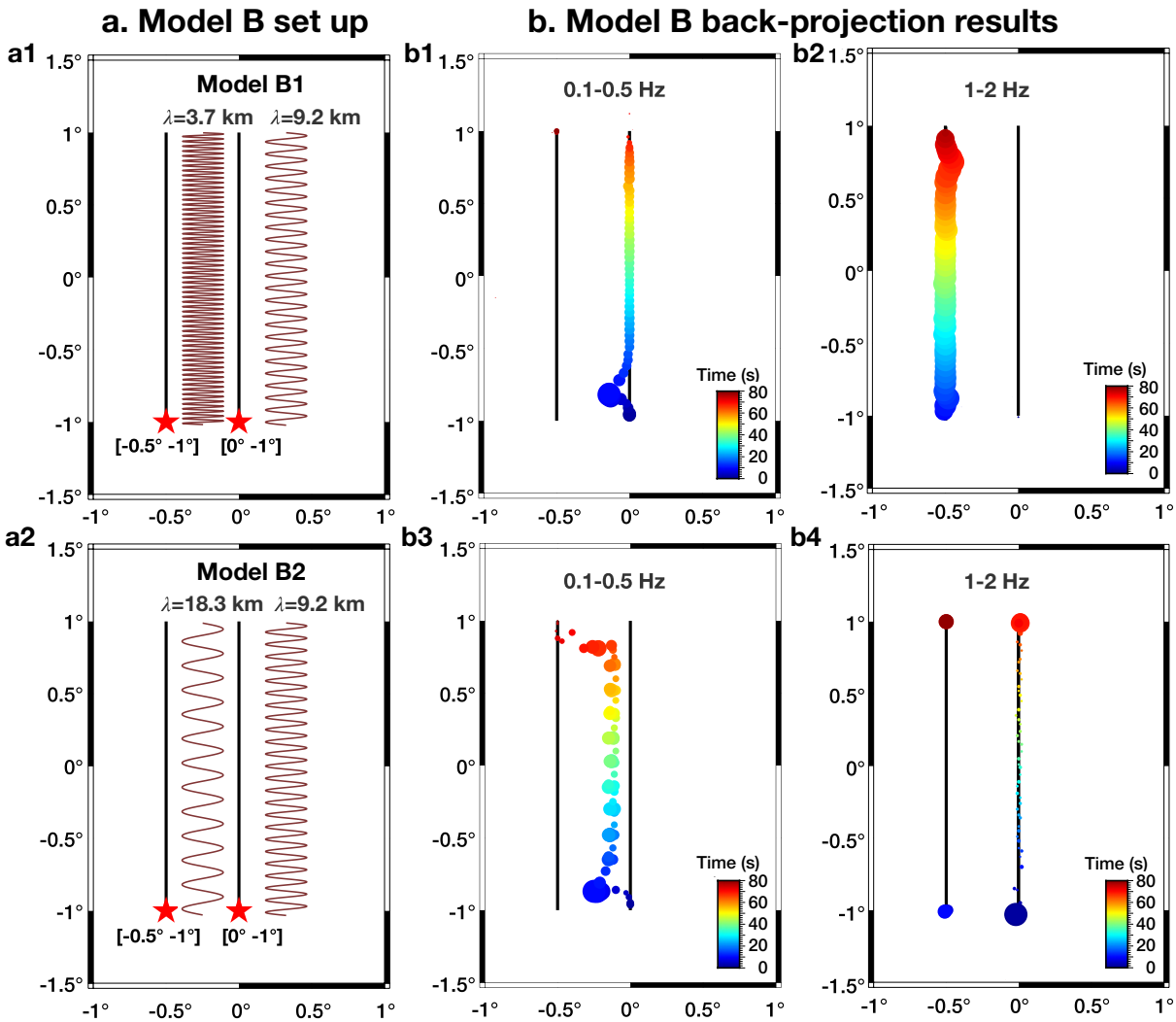

Figure 4. Models of two simultaneous rupture branches (Model B) and their back-projection results. (a) Schematics of 2 kinematic source models with rupture propagating simultaneously and unilaterally on two parallel faults from the south to north. (b) The rupture process imaged by the back-projection for both models described in (a), using frequency filtered (0.1–0.5 Hz and 1–2 Hz) synthetic seismograms.

3.4. Frequency-Dependent Back-Projection Analysis for the Simultaneous, Unilateral & Heterogeneous Ruptures on Two Parallel Faults (Model B)

Back-projection studies often reveal distinct rupture features when using seismic data that are filtered in different frequency ranges, especially for subduction earthquakes where the frequency content of the rupture process appears to be depth dependent (e.g., Kiser & Ishii, 2011; Kiser & Ishii, 2017; Koper et al., 2011; Yao et al., 2013). In addition, for complex ruptures with multiple and simultaneous rupture branches/fronts, a single array tends to capture only part of the rupture at a certain frequency band, and leave other parts of the rupture process unseen. Those "hidden" ruptures can also have significant seismic moment compared to the ruptures revealed using back-projection (e.g., Galetzka et al., 2015; Meng et al., 2016).

To investigate this phenomenon, we model simultaneous ruptures propagating unilaterally from the south to north on two N-S striking faults. We refer to this model as Model B. As shown in Figures 1c3 and 4a, the two parallel faults have the same length, and are 0.5° away from each other. We refer to the rupture starting at [0.5°W −1°] as the "left rupture" and the rupture starting at [0°–1°] as the "right rupture".

As in Model A2, peak slip rate (1 m/s) and fault-local strike (0°) are constant on both faults, average rupture velocity is 3 km/s, and the normalized variation amplitude α is 0.3. Only the variation wavelength λ is different

on the two faults, meaning that both ruptures have the same seismic moment. A summary of model parameter settings are shown in Table S2 and Figure 4a.

In Model B1 (Figure 4a1) we set the heterogeneity wavelength λ to 3.7 and 9.2 km on the left and right faults, respectively. We then implement back-projection with the synthetic seismograms filtered in 0.1–0.5 Hz and 1–2 Hz bands. The results are shown in Figures 4b1 and 4b2, which also demonstrate frequency-dependent rupture imaging. When filtering in the frequency range 0.1–0.5 Hz, back-projection captures the rupture propagation on the right fault, which has large λ (9.2 km). In contrast, back-projection in the 1–2 Hz range captures the rupture process on the left fault, with its shorter λ (3.7 km).

Model B2 increases λ on the left fault to 18.3 km and keeps $\lambda = 9.2$ km on the right fault. The 1–2 Hz back-projection in this case captures the rupture on the right fault, which now has the shorter λ (9.2 km). Back-projection between 0.1 and 0.5 Hz images the rupture propagation not on either of the two parallel faults, but rather in between (longitude ~0.13°W) and closer to the right branch rupture. The Model B results support the idea that if multiple faults rupture simultaneously, back-projection tends to image the rupture(s) whose heterogeneity wavelength matches the filtered seismogram frequencies. If the heterogeneity wavelength on simultaneous rupture branches results in comparable amplitude signals in the filtered frequency range, the back-projection may locate the rupture sources in between the simultaneous sources when the array resolution is not high enough.

3.5. Frequency-Dependent Back-Projection Analysis for the Simultaneous, Bilateral & Heterogeneous Ruptures on One Single Fault (Model C)

The deployment of global seismic networks allows back-projection analysis for a given earthquake using arrays in multiple locations. Back-projection results of arrays at different azimuth relative to the source region can reveal distinct rupture features, even if the seismic data are filtered in the same frequency range (e.g., Zhang et al., 2016; Li, 2019). These array-dependent results suggest the rupture directivity may also play an important role in back-projection when imaging complex earthquakes.

To investigate the effect of rupture directivity on back-projection results, here we model bilateral rupture on a single fault (Model C; Table S2, Figure 1c2). Like Model A2, the peak slip rate (1 m/s) and fault-local strike (0°) are both invariant. The rupture starts at [0° 0°] in the middle of the fault and propagates bilaterally to the north ([0° 1°N]) and south ([0° 1°S]) simultaneously. The rupture velocity varies as a harmonic sine function, with an average rupture velocity of 3 km/s, and a normalized variation amplitude α of 0.2. Variation wavelength λ is the same in both rupture directions: 4.6 km in Model C1 and 1.8 km in Model C2 (Table S2, Figure 5a). Therefore, the bilateral ruptures propagate symmetrically relative to the center of the fault, leading to identical seismic moment release in the north- and south-propagating ruptures. Since we use a seismic array in the northeast direction of the source region, we refer to the north-propagating rupture as the "toward" rupture, and the south-propagating rupture as the "backward" rupture.

Figure 5b shows back-projection results of Model C. For Model C1, the back-projection captures the backward rupture (propagating to the south) when filtering in 0.1–0.5 Hz (Figure 5b1). For the toward rupture (propagating to the north), only the stopping phase is located. In a higher frequency range 1–2 Hz, only the toward rupture is imaged by back-projection (Figure 5b2). For Model C2, with a smaller λ, the back-projection results of 1–2 Hz captures the backward rupture (Figure 5b3). The reversal of the tracked rupture direction in different frequency ranges suggests that the rupture directivity effect can also result in frequency-dependent back-projection results. This result is also consistent with our previous experiments showing that a shorter heterogeneity wavelength generates more high-frequency radiation.

4. Theoretical Relations Between Heterogeneity Wavelength and Frequency- and Array-dependent Back-Projection Results, and Implications for the 2019 M7.6 New Ireland Earthquake

The synthetic experiments above show that both rupture heterogeneity wavelength and directivity can cause frequency-dependent back-projection results. Although we cannot distinguish the different types of heterogeneity based on the back-projection results alone, we may still be able to extract useful information about the rupture characteristics, such as the heterogeneity wavelength. In the following section, we develop a theoretical relation

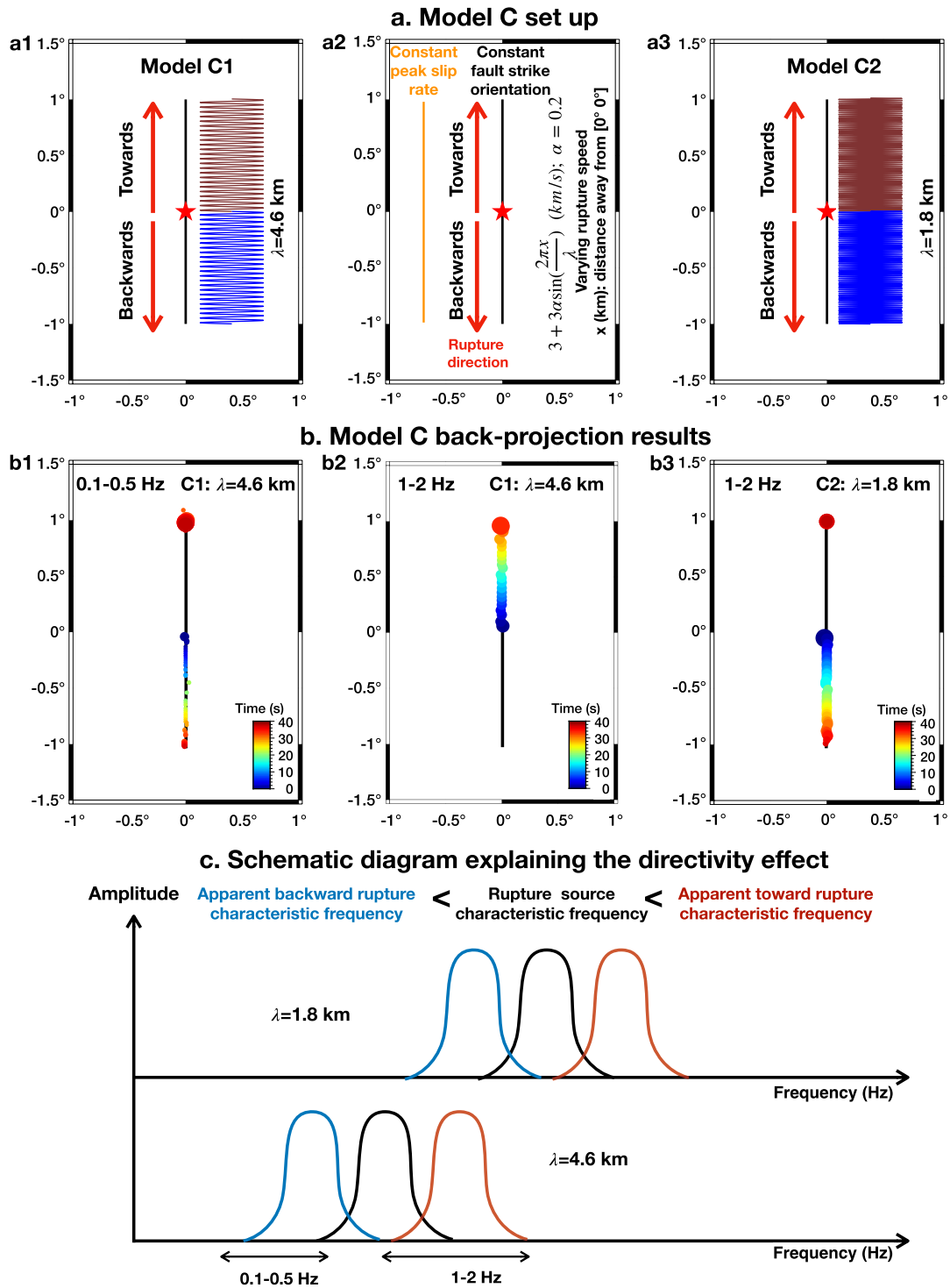

Figure 5. Bilateral rupture models (Model C) and the back-projection results. (a) Model parameter settings (a2) and the rupture velocity variation in Model C1 (a1) and C2 (a3). (b) The frequency-dependent back-projection results for the "bilateral rupture" experiments. It suggests both the heterogeneity wavelength and rupture directivity can result in frequency-dependent back-projection results. (c) Schematic diagram that illustrates the spectrum analysis for the bilateral experiments. The horizontal axis represents the frequency and vertical axis indicates the amplitude. The black curves show the spectrum with no directivity effect. The red and blue curves represent the spectrum for the "toward rupture" and "backward rupture" (see definition in Section 3.5), respectively. The center of curvature of each curve corresponds to its characteristic frequency.

based on Doppler theory to explain our synthetic results and apply it to analyze the 2019 M7.6 bilaterally rupturing New Ireland earthquake.

4.1. Theoretical Relation Between the Heterogeneity Wavelength and Seismogram Frequency

We seek a quantitative relationship between the rupture heterogeneity wavelength λ and its apparent corresponding characteristic frequency f_h associated with a peak amplitude in the recorded spectrum at the array location. We start with the Doppler effect, which describes the change in frequency of a wave due to the relative motion between an observer and the wave source (Gothard & Rosen, 2010, pp. 154–156):

$$f_h = \left(\frac{c \pm v_r}{c \pm v_s}\right) f_{h0}, \tag{7}$$

where f_{h0} is the emitted frequency in the source frame, and f_h represents the observed frequency at the receiver. c is the wave propagation velocity in the medium. v_r is the velocity of the receiver relative to the medium along the travel path, added to c if the receiver is moving toward the source, and subtracted when moving away from the source. v_s is the velocity of the source relative to the medium along the travel path, added to c if the source is moving away from the receiver, and subtracted if the source is moving toward the receiver.

In our experiments, the characteristic frequency f_{h0} at the source is directly related to the source properties. For real earthquakes, f_{h0} can be a dominant frequency instead of a single frequency as in our experiments. The characteristic frequency is proportional to the local average rupture velocity V_{rup} and inversely proportional to the heterogeneity wavelength λ_{h0} at the source, so $f_{h0} = V_{rup}/\lambda_{h0}$. For back-projection analysis with P waves, c is the P wave velocity, $c = V_p$. The receiver is not moving, so $v_r = 0$, and v_s is the component of the rupture propagation velocity on the fault projected onto the P wave take-off direction, $v_s = -V_{rup}\cos\theta$, in which θ is the angle between the take-off ray of the P wave and the source rupture direction. Substituting these relationships into Equation 7, we obtain:

$$\begin{aligned} f_h &= \frac{1}{\lambda_{h0}}\left(\frac{1}{V_{rup}} - \frac{\cos\theta}{V_p}\right)^{-1}, \quad \text{or,} \\ \lambda_{h0} &= \frac{1}{f_h}\left(\frac{1}{V_{rup}} - \frac{\cos\theta}{V_p}\right)^{-1}. \end{aligned} \tag{8}$$

Equation 8 suggests that the apparent characteristic frequency f_h recorded at the array depends on both the source heterogeneity wavelength λ_{h0} and the rupture directivity. There is an inverse relationship between λ_{h0} and f_h: a higher/lower frequency back-projection tends to capture the rupture with shorter/longer λ_{h0}. When rupture propagates toward the array, $\cos\theta$ will have a positive value. In this case, f_h at the array is higher than the intrinsic characteristic frequency f_{h0} ($f_{h0} = V_{rup}/\lambda_{h0}$; red shift in Figure 5c). Conversely, when rupture propagates away from the array, $\cos\theta$ will have a negative value, and f_h at the array is lower than the intrinsic characteristic frequency f_{h0} (blue shift in Figure 5c).

4.2. Evaluation of the Theoretical Relation With Synthetic Experiments

We apply Equation 8 to quantitatively explain the back-projection results in our synthetic experiments, particularly the relationship between the apparent characteristic frequency f_h at the array and the heterogeneity wavelength λ_{h0} of the rupture.

In model A5, the rupture propagates unilaterally on a single fault from south to north, with different heterogeneity wavelengths. Based on the array and model settings, the θ in all experiments of model A5 would be 49.2°. The values of λ_{h0} are 1.6, 2.0, 2.3, 2.8, 3.7, 4.6, 9.2, 18.3, 27.5, 55 and 220 km, resulting in corresponding f_h of 2.91, 2.36, 2.02, 1.68, 1.26, 1.01, 0.50, 0.25, 0.17, 0.08 and 0.02 Hz, respectively. When filtering around the matched frequency range, the corresponding λ_{h0} rupture will produce higher amplitude seismograms, leading to stronger beam energy in the back-projection results. The seismogram amplitude decays when filtering in a range away from the f_h. We calculate the λ_{h0} correlated with the central frequency (0.3, 1.5 and 4 Hz) of the three frequency ranges (0.1–0.5, 1–2 and 3–5 Hz) that we used in our experiments. The corresponding λ_{h0} are plotted as red dashed lines in Figure 3. We find that the corresponding central λ_{h0} matches with the strongest beam energy in the results, as the predicted λ_{h0} are close to the center of the blue-shaded area in Figure 3. A slight deviation is

observed in 3–5 Hz results. We argue that this discrepancy is due to the fixed slip rate function duration (1 s) in the model setup (see Discussion Section 5.2.2).

For Model B, two simultaneous ruptures propagate unilaterally from the south to north on two parallel faults, with a different heterogeneity wavelength on each fault. Our results show that back-projection tends to track only a single rupture branch, depending on the heterogeneity wavelength and filtered frequency range. These results can also be explained by Equation 8: the three λ_{h0}, 3.7, 9.2, 18.3 km used in Model B correspond to f_h of 1.26, 0.50 and 0.25 Hz, respectively. Thus in Model B1, the left segment has $\lambda_{h0} = 3.7$ km ($f_h = 1.26$ Hz) and the right branch has $\lambda_{h0} = 9.2$ km ($f_h = 0.5$ Hz); therefore, the left segment rupture is captured by the back-projection in 1–2 Hz, while the right branch rupture is captured in 0.1–0.5 Hz. In Model B2, the left segment has $\lambda_{h0} = 9.2$ km ($f_h = 0.5$ Hz) and the right branch has $\lambda_{h0} = 18.3$ km ($f_h = 0.25$ Hz). When filtering in 0.1–0.5 Hz, both f_h fall within this range, and the back-projection results show rupture imaged in between the two segments. When filtering in 1–2 Hz, significantly higher than either f_h (0.25 and 0.5 Hz), the amplitude of the left rupture with $\lambda_{h0} = 18.3$ km ($f_h = 0.25$ Hz) is farther away from the filter's center, so the back-projection preferentially captures the right rupture with $\lambda_h = 9.2$ km ($f_h = 0.5$ Hz).

In Model C, the rupture propagates bilaterally and simultaneously north and south on a single fault. The north branch rupture propagates toward the array with $\theta = 49.2°$ and the south branch rupture propagates away from the array with $\theta = 131°$. In Model C1, λ_{h0} is 4.6 km, so the toward rupture has $f_h = 1.01$ Hz and the backward rupture has $f_h = 0.48$ Hz. Therefore, when filtering in 1–2 Hz, back-projection tracks the toward rupture (north branch); while when filtering in 0.1–0.5 Hz, back-projection tracks the backward rupture (south branch). In Model C2, λ_{h0} is 1.8 km, so the toward rupture has $f_h = 2.6$ Hz and the backward rupture has $f_h = 1.2$ Hz. Therefore, when filtering in 1–2 Hz, back-projection tracks the backward rupture (south branch), instead of the toward (north branch) rupture.

We use the schematic diagram in Figure 5c to qualitatively illustrate the relation between the radiation and apparent frequency due to the Doppler effect. The upper plot shows the spectra of the Model C2 ($\lambda_{h0} = 1.8$ km), and the lower plot shows the spectra of Model C1 ($\lambda_{h0} = 4.6$ km). The black, red and blue curves represent the radiation spectra of the rupture without the Doppler effect ($\cos\theta = 0$), the toward rupture ($\cos\theta > 0$), and the backward rupture ($\cos\theta < 0$), respectively. Radiation spectra of the starting and stopping phases are not displayed. Since the characteristic frequency $f_{h0} = V_{rup}/\lambda_{h0}$ and V_{rup} is the same in each model, the "No-Doppler" spectrum is at a higher characteristic frequency for the $\lambda_{h0} = 1.8$ km model (upper plot) than the $\lambda_{h0} = 4.6$ km model (lower plot). For both models, the toward rupture results in higher f_h and the spectrum shifts to a higher frequency domain than the "No-Doppler" spectrum, while the spectrum of the backward rupture will shift to a lower frequency. This explains that in Model C1 ($\lambda_{h0} = 4.6$ km), when filtering in 1–2 Hz, the back-projection images the toward rupture (north branch; Figure 5b1), and when filtering in the 0.1–0.5 Hz, the back-projection images the backward rupture (south branch; Figure 5b2). In our setup, the backward rupture in Model C2 ($\lambda_{h0} = 1.8$ km) has a similar frequency range of the spectrum as the toward rupture in Model C1 ($\lambda_{h0} = 4.6$ km). It explains why in Model C2, when filtering between 1 and 2 Hz, the back-projection tracks the backwards rupture (south branch), not the toward rupture (north branch) in Model C1. We note that the apparent characteristic frequency shift quantitatively depends on rupture velocity itself (Equation 8). We also note that expressing slip rates as asymmetric Yoffe function (Tinti et al., 2005) does not change f_h for the corresponding λ_{h0} when using the symmetric cosine function defined in Equation 1 (Figure S7 in Supporting Information S1). Therefore, the choice of the slip rate function should not imprint on our analysis. Further discussion can be found in Section 5.4.4.

4.3. Application to the 2019 Mw7.6 New Ireland Earthquake

The 14 May 2019 Mw 7.6 New Ireland Earthquake occurred in Papua New Guinea. It ruptured bilaterally to the northwest and southeast along the highly active Weitin fault (Chen et al., 2019; Tregoning et al., 1999), consistent with the left-lateral strike-slip W-phase focal mechanism (USGS, https://earthquake.usgs.gov/earthquakes/eventpage/us70003kyy/moment-tensor, last access in June 2021). The similarity between this earthquake and our synthetic Model C makes this event an ideal case to test our theoretical relation against a natural earthquake. However, depth phases (pP and sP), which are not considered in our synthetic experiments, may affect the application of our theoretic analysis to the New Ireland earthquake. The radiation pattern coefficient indicates the average pP-to-P amplitude ratio is smaller than 0.5 at both arrays (Figure S8 in Supporting Information S1) that we select to perform back-projection: the China array to the northwest and the Alaska array to the northeast

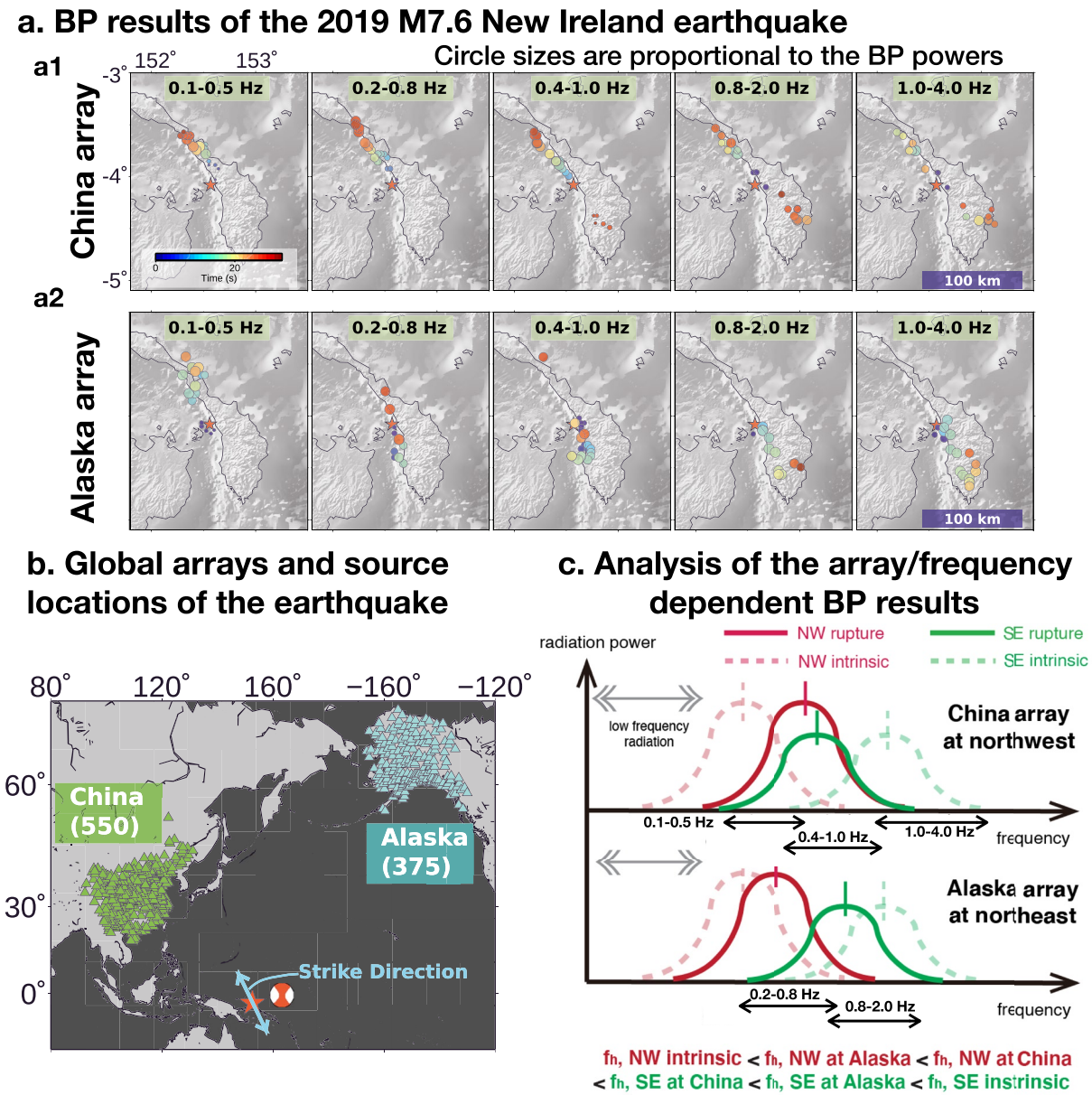

Figure 6. Frequency- and array-dependent back-projection results of the 2019 M7.6 New Ireland earthquake. Different rupture features are captured by different arrays in different frequency ranges. (a) Multiple frequency ranges of filtered back-projection results using the China and Alaska array located at different azimuths relative to the source rupture region. (b) Global map view showing the two arrays and the rupture source region. Blue line with two arrowheads demonstrates the strike orientation of the bilaterally ruptured Weitin fault. Beachball shows the W-phase focal mechanism (from USGS) of this event. (c) Schematic diagram showing the inferred high-frequency spectra of signals received by both arrays from the northwest and southeast direction rupture sources.

(Figure 6b). The effects from depth phases are reduced in the high-frequency signal (~1 Hz) that back-projection utilizes, compared to lower frequency methods such as finite-fault inversion (usually <0.2 Hz). This is because the paths of depth phases penetrate through near-surface structures with strong attenuation, and thus lose more high-frequency energy than P waves (Ammon et al., 2020). For strike-slip earthquakes specifically, the sP phase can be a predominant phase in the P wave train. However, the finite fault inversion of this event from the USGS shows that the rupture depth for this event is shallow and does not extend over a great depth range. We here assume that the complete P wave train (including pP and sP phases) can be treated as the rupture source. Therefore, we argue that the depth phase of the New Ireland earthquake will not significantly affect our back-projection analysis.

Figure 6a shows the back-projection results, with the same back-projection method as in our synthetic experiments applied at five different frequency bands: 0.1–0.5, 0.2–0.8, 0.4–1.0, 0.8–2.0 and 1.0–4.0 Hz. We also apply the Multitaper-MUSIC back-projection analysis (e.g., Bao et al., 2019; Meng et al., 2016) to this earthquake with similar results (Figure S4 in Supporting Information S1), indicating that our conclusions do not depend on the specifics of the method used.

Different frequency bands produce distinct results. The China array at 0.4–1.0, 0.8–2.0 and 1.0–4.0 Hz, as well as the Alaska array at 0.2–0.8 Hz, can track both branches of the bilateral rupture, while others cannot. Even among the results that track both branches, the northwest (NW) rupture and the southeast (SE) rupture can have different back-projection beam power. These frequency- and array-dependent results can be deciphered via the theoretical analysis from the synthetic results. First, the relative emitted frequency f_{h0} level of the NW and SE ruptures can be estimated by comparing the back-projection results using the same array in different frequency bands. Both the China array and Alaska array show that more NW branch features are imaged when filtering in a lower frequency band. When the frequency increases, the back-projection in both arrays capture more SE branch rupture features. This result indicates that while the radiation from the fault is likely broadband, the NW rupture might have an intrinsic dominant characteristic frequency f_{h0} lower than the SE rupture.

A further comparison of the results between the two arrays can help us better constrain the frequency-related energy radiation of the two rupture branches. In the China array results (Figure 6a1), the NW rupture generally has stronger beam power than the SE rupture. Conversely, in the Alaska array results (Figure 6a2), the SE rupture is often the stronger branch, except in the two lowest-frequency back-projection images. The difference between the two arrays is most obvious in the frequency range 0.4–1 Hz, where the China array almost captures only the NW rupture, while the Alaska array primarily captures the SW rupture.

We may understand the above comparison through our theoretical relation in Equation 8. We assume the rupture direction is along the strike direction of the Weitin fault, with the NW and SE branches striking 319° and 139°, as suggested by the USGS focal mechanism analysis. To estimate the angle θ between the P wave take-off ray and the rupture propagation directions, we use the TauP Toolkit (Crotwell et al., 1999) to compute the P wave raypath from the earthquake hypocenter to the geometry center of the array using the 1D IASP91 velocity model. The results show the NW and SE ruptures have θ equal to 66° and 114° for the China array and 82° and 98° for the Alaska array, respectively. It implies that the NW rupture is propagating toward and the SE rupture is propagating backwards for both arrays.

These array- and frequency-dependent back-projection observations help us to infer the intrinsic and apparent spectra of the NW and SE rupture branches. The results suggest the NW rupture has an intrinsic spectrum in a lower frequency and higher amplitude domain compared to the SE rupture. Since the China array has higher absolute values of $\cos\theta$ than the Alaska array for both the toward and backward ruptures, we expect a stronger Doppler effect in China array. Thus, the apparent spectra of the China array will be shifted further from the intrinsic source spectrum than those of the Alaska array-to a lower frequency domain for the SE rupture, and to a higher frequency domain for the NW rupture.

Based on our synthetic model analyses and previous generic inferences, we formulate a schematic model to quantitatively analyze the spectra of this bilateral rupture event (Figure 6c). The intrinsic source spectra (dashed lines) are the same for both arrays. In the apparent spectrum at the China array, shown as solid lines in the top panel of Figure 6c, the NW rupture branch has a higher amplitude than the SE branch in lower frequency bands (0.1–0.5, 0.2–0.8 Hz). Thus, back-projection captures only the rupture to the NW in these low-frequency bands. However the difference of spectrum amplitudes diminishes as the frequency increases, which is why the China array starts to image the SE rupture at higher frequency bands (0.4–1, 0.8–2 Hz; Figure 6a), but with lower beam power. Both directions are imaged with comparable beam powers at the highest frequency range (1–4 Hz). Due to a weaker Doppler effect, the two apparent spectra at the Alaska array, shown as solid lines in the bottom panel of Figure 6c, are separated with a smaller overlap of the NW and SE ruptures. This results in the radiation of the NW rupture branch being still dominant but in a lower frequency domain than the China array, and the SE branch will have higher amplitude in the high frequency. In the frequency range of 0.1–0.5 Hz, the Alaska array only tracks the NW rupture propagation, while both directions are imaged with comparable beam powers in 0.2–0.8 Hz, and only the SE rupture is captured in the higher frequency bands (0.4–1, 0.8–0.2, 1–4 Hz).

If the rupture propagation velocity is well constrained by other means, we may use Equation 8 to estimate the characteristic heterogeneity wavelength λ_{h0} for both the NW and SE rupture. Quantifying accurate rupture parameters for this earthquake requires a comprehensive synthesis of observations and models, which is beyond the scope of this paper. Instead, we use this earthquake as an example to demonstrate how such a heterogeneity wavelength analysis can be applied to interpret frequency- and array-dependent back-projection results for real earthquakes. Our spectral model would suggest that the dominant emitted frequency is about 0.25 Hz for the NW rupture and about 1 Hz for the SE rupture. If the rupture propagation velocity for both branches were 3 km/s, the NW rupture would have a dominant heterogeneity wavelength $\lambda_{h0} = 3/0.25 = 12$ km while the SE rupture would have a dominant heterogeneity wavelength $\lambda_{h0} = 3/1 = 3$ km.

We note that in this case there is no clear expression of any fault structural complexity in optical image measurements as well as geological mapping, which show quite linear fault geometry (Chen et al., 2019; Lindley, 2006). However, high stress-drops have been inferred off-shore, where a previous Mw 8.0 rupture terminated in 2000, perhaps due to locally more intense dynamic weakening. Additionally, large strike-slip earthquakes on very linear fault segments may rupture at speeds faster than the shear wave velocity (Bouchon & Vallée, 2003; Dunham & Archuleta, 2004). Variations in rupture velocity and other types and wavelengths of heterogeneity may be a plausible hypothesis guiding more detailed analyses. Nevertheless, the robustness of such analysis procedures can be tested against other earthquakes with a synthesis of observations. If this procedure is shown effective, it might be applied to estimate the first-order features of dominant heterogeneity wavelength in large earthquakes.

5. Discussion

5.1. Beam Power, Moment Rate Function, and Far-Field P Wave Radiation

Back-projection beam power is typically assumed to represent the amplitude of high-frequency radiation at the rupture front (e.g., Meng et al., 2016). In back-projection studies, beam power is often used to infer the moment rate function, or source time function, a physical quantity that is commonly used to characterize earthquakes (e.g., Meier et al., 2017; Ye et al., 2016). The moment rate function can be defined as the integrated moment density rate across the slipped fault, and is different from the "apparent source time function" which is obtained by deconvolution of empirical Green's functions from seismograms (Vallée et al., 2011). In addition, the moment rate function has a clear relation with the far-field body wave radiation (Equation 2). If an earthquake source can be treated as a point source, its far-field P wave displacement or velocity amplitude will be proportional to the point source moment rate or acceleration function. This assumption is reasonable as long as the seismic wave wavelength under consideration is longer than the source dimension. Intuitively, one might assume that back-projection beam power can be related to the moment rate function, and such a comparison for real earthquakes has been done for many observational back-projection studies (e.g., Lay et al., 2010; Tan et al., 2019). However, these two results do not always correlate with each other, and their relation is still an open question.

Here we attempt to address this issue using our synthetic results. Figure 7 shows the normalized moment rate function (red curves in the left column), the normalized beam power (black curves in the left column), and the far-field P wave vertical velocity seismograms (unfiltered in the middle column, filtered to 1–2 Hz in the right column) for Models A1, A2, A3, and A4. All models are Haskell-type kinematic models, so their moment rate functions all have a sharp increase and decrease at the start and termination of the rupture. These sharp changes of moment rate function lead to large moment acceleration, which generate large pulses at the beginning and end of the P wave train (starting and stopping phases), and cause large beam power.

As shown in Figure 7a, the homogeneous rupture model (Model A1) has a flat moment rate between the starting and stopping phase, so its far-field P wave seismogram has insignificant amplitudes during the rupture process. Models A2 (Figure 7b) and A3 (Figure 7c) have heterogeneous rupture, with varying rupture velocity and maximum slip rate along the fault, respectively. The spatial variation of rupture velocity and maximum slip rate causes a temporal fluctuation in the moment rate function, which in turn results in seismogram fluctuation and causes high beam power in a certain frequency band. In contrast to Models A2 and A3, variable moment rate function does not explain the far-field radiation in Model A4 (varying fault-local strike, Figure 7d). Model A4's moment rate function is exactly the same as for Model A1, but the rupture generates seismogram fluctuations similar to Model A2 and A3, and results in high beam power.

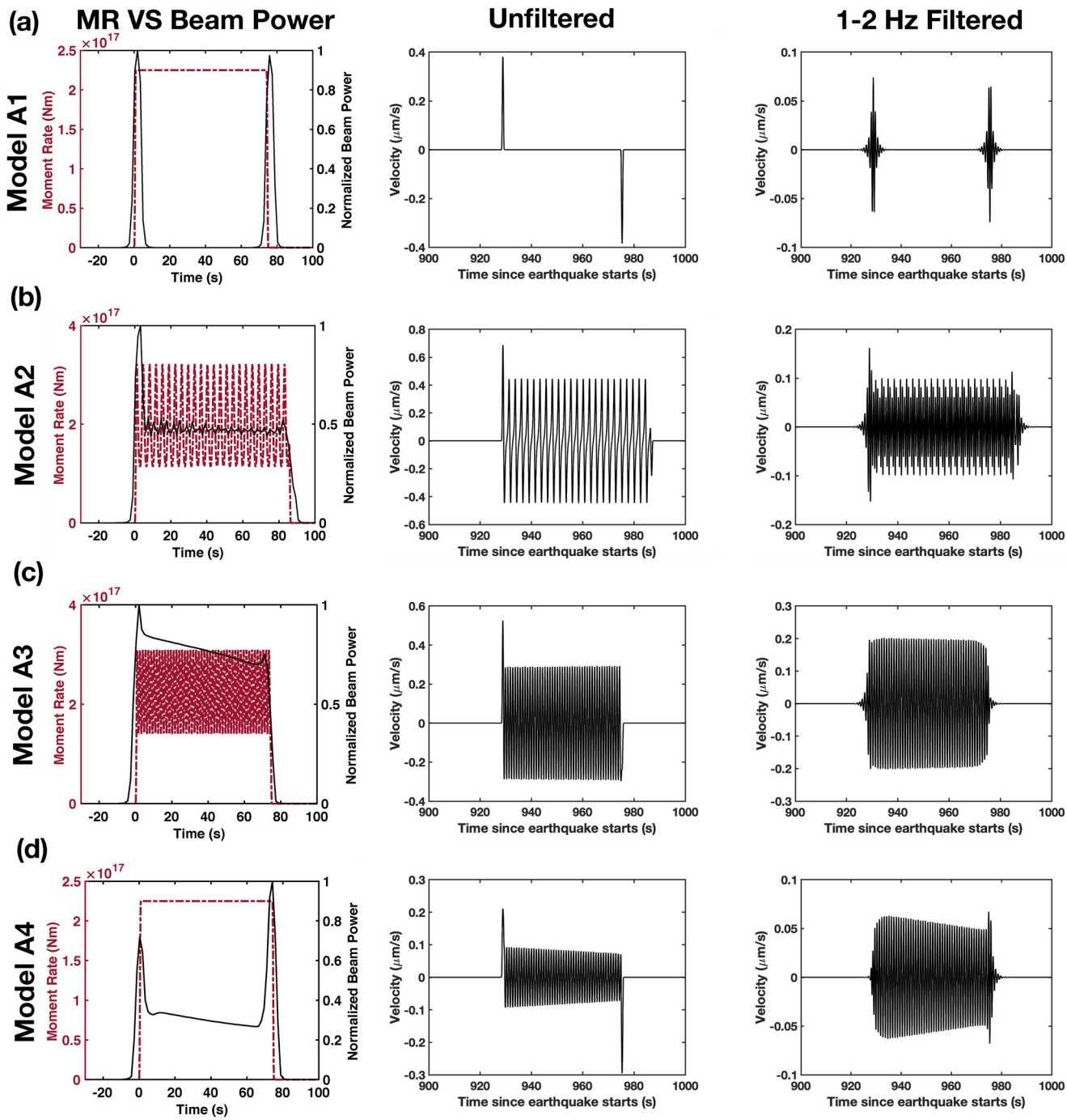

Figure 7. The normalized moment rate function, normalized beam power, and synthetic seismograms for (a) Model A1, (b) Model A2, (c) Model A3, and (d) Model A4. In our synthetic experiments, each point source has an effective width of 5 km. In that case, the absolute value of the maximum moment rate function is slightly different from each model, but does not affect our analysis. Left column: comparisons between moment rate function (red curves) and beam power (black curves). Middle column: unfiltered vertical velocity seismograms at longitude 35.26°, latitude 34°. Right column: seismograms filtered in 1–2 Hz. Model A4 (varying fault-local strike) has no fluctuation in the moment rate function, but there is still fluctuation in the seismogram, which is caused by the spatial variation of the radiation pattern factor A^{FP} in Equation 2.

We conclude that the back-projection beam power function, in principle, should be more related to the moment acceleration function rather than the moment rate function. In addition, since back-projection analysis is performed in a predetermined frequency range, any type of rupture heterogeneity with corresponding wavelength that can induce a fluctuation in the moment rate function (and thus moment acceleration function) within the

given frequency band, should be able to cause high beam power. However, the mechanisms that cause high beam power are not limited to the moment-rate function. In Model A4, variation of fault-local strike causes a variation of the radiation pattern factor (A^{FP} in Equation 2) along the fault, which also causes high frequency signals. In the real world, a change in fault strike could well be associated with a variation in moment rate function (e.g., through a change in the resolved shear and normal stresses). However, synthetic Model A4 indicates, at least in the kinematic sense, that a variation in fault strike by itself can generate high-frequency radiation, without a corresponding change in stress, slip, or rupture velocity. We hypothesize that other types of spatial variations (e.g., slip rise time, slip rake, local P wave velocity structure, attenuation structure) related to P wave radiation can also cause high-frequency signals. We will perform a simple analytical analysis for these hypotheses in the next section.

5.2. Relating Back-Projection Beam Power to Slip and/or Heterogeneity

5.2.1. Comparison With Previous Theoretical Studies

Since the first application of the back-projection method to the 2004 Sumatra-Andaman Earthquake (Ishii et al., 2005), researchers have attempted to theoretically relate the back-projection beam power to slip-related physical source properties (slip, slip rate, or slip rate acceleration) that are relatively well-defined. Based on two back-projection assumptions: 1. waveforms due to slip on the fault other than the target source grid will be canceled out, and 2. the stacked Green's function is resembling a delta function, Fukahata et al. (2014) conclude the back-projection images represent the slip motion on the fault. Okuwaki et al. (2019) show the back-projection signal intensity can be related to the slip motion on the fault by modifying the normalizing factor to cancel out the signal amplitude variants due to the depth-dependent Green's functions. Using the displacement synthetic waveforms, Yin and Denolle (2019) imply that if corrected for attenuation, the BP images derived from raw seismic data, are proportional to the slip-rate field after a spatial smoothing, which can be parametrized by the array response related resolution matrix $F(\omega)$. All these studies indicate a (direct or blurred) relationship between the back-projection images or the beam power (peaks) and the slip motion on the fault.

In contrast, in many of our experiments, a location on a fault could be experiencing high slip, slip rate, and slip acceleration, while still displaying insignificant BP beam energy. In our study, the synthetic experiments show that the frequency-dependent back-projection beam power amplitude (peak) is related to the wavelength spectrum of rupture heterogeneities on the fault, and modulated by the rupture directivity relative to the array azimuth. We argue that our results and their interpretation are due to the characteristics of the typical slip acceleration profile, in which both high-acceleration and high-deceleration co-exist near the rupture front. Previous studies indicate that the back-projection beam energy represents a spatial average of the slip field (slip, slip rate, or slip rate acceleration), weighted by the Green's function over an area near the back-projected location at a certain time. However, during the rupture propagation, a spatial average of the slip acceleration profile with both acceleration and deceleration may cancel out these quantities in the far-field velocity waveform, resulting in an insignificant integral even if the maximum absolute slip acceleration is high. One example is the homogeneous model in our synthetic experiments, where the absolute peak slip rate is the same as other heterogeneous models, but the beam power is insignificant and back-projection images do not show any correlation with the slip motion on the fault. In fact, the acceleration and deceleration contributions would tend to cancel out near the rupture front, since fault slip rate will always start and end at zero. In other words, the radiation wavefield of a propagating rupture front may exhibit destructive interference, severing the direct connection between the slip process and the back-projection beam power.

5.2.2. Analytical Derivation for the Destructive Interference Effect

A complete cancellation of the far-field signal can be analytically shown for a 1D rupture model assuming homogeneous rupture velocity and homogeneous maximum slip rate. Let's examine a simple 1D rupture model such as Model A, except that we set the slip rate shape function to have a general form as follows:

$$f(t) = \begin{cases} f(t) & \text{if } t \in [0, T] \\ 0, \text{otherwise} & \end{cases} \tag{9}$$

Based on the ARF, which is also indicated by the resolution matrix F(w) defined in Yin and Denolle (2019), the back-projection stacked beam amplitude at a certain location at a certain time can be related to the integral of the spatially weighted slip acceleration near that location. Thus, for the homogeneous 1D line rupture, we have,

$$s\left(\xi^j, t\right) \sim \int_{\xi^j-\Delta\xi}^{\xi^j+\Delta\xi} A\left(\xi-\xi^j\right) G(\xi)\ddot{D}(\xi, t)\mathrm{d}\xi, \tag{10}$$

in which $s(\xi^j, t)$ is the stacked velocity seismogram amplitude at location ξ^j, and $G(\xi)$ is a Green's function related term. $A(\xi - \xi^j)$ is a weighting function that depends on the shape of the ARF. For simplicity, $A(\xi - \xi^j)$ can be treated as a constant in the integration range (a boxcar function). $\Delta\xi$ is the area (distance in 1-D) range near ξ^j where source signals can stack coherently. Fundamentally, $\Delta\xi$ is related to the resolution of ARF (Rost & Thomas, 2002), and its value depends on both the chosen frequency range and rupture directivity. $D(\xi, t)$ is the spatial-temporal distribution of slip.

To examine the slip acceleration profile near the rupture front, we assume the fault at ξ^j starts to slip at time t^0(rupture time). The corresponding slip rate function at the location near ξ^j can be written as,

$$\dot{D}(\xi, t) = \dot{D}_{peak}(\xi) f\left(t - t^0 + \Delta t\left(\xi, \xi^j\right)\right), \tag{11}$$

where $\dot{D}_{peak}(\xi)$ is the peak slip rate at location ξ, and $\Delta t(\xi, \xi^j)$ is the rupture time difference between ξ and ξ^j. Then, we take the time derivative of Equation 11, substitute it into Equation 10, examine the expression at $t = t^0$, and we have,

$$s\left(\xi^j, t^0\right) \sim \int_{\xi^j-\Delta\xi}^{\xi^j+\Delta\xi} G(\xi)\dot{D}_{peak}(\xi) f'\left(\Delta t\left(\xi, \xi^j\right)\right)\mathrm{d}\xi. \tag{12}$$

Let's now consider the most simple case where the slip is homogeneous and the rupture propagation velocity is a spatial constant V_{rup}, so $\Delta t(\xi, \xi^j)$ can be written as,

$$\Delta t\left(\xi, \xi^j\right) = \frac{\xi - \xi^j}{V_{rup}}. \tag{13}$$

In this case, the integration in Equation 12 can be carried out because the integral kernel contains only the derivative of function f, and the mapping function from the rupture time difference $\Delta t(\xi, \xi^j)$ to the space ξ is linear. Then, the stacked beam amplitude can be expressed as:

$$\begin{aligned} s\left(\xi^j, t^0\right) &\sim G \times \dot{D}_{peak} \times \int_{\xi^j-\Delta\xi}^{\xi^j+\Delta\xi} f'\left(\frac{\xi-\xi^j}{V_{rup}}\right)\mathrm{d}\xi \\ &= V_{rup} \times \dot{D}_{peak}\left(\frac{\xi}{V_{rup}}\right)\Bigg|_{\xi=-\Delta\xi}^{\xi=\Delta\xi}. \end{aligned} \tag{14}$$

As Equation 14 shows, the integral of the slip rate function f' in Equation 12 can be expressed as the slip rate difference between two points in time: one at $t = f\left(\frac{\Delta\xi}{V_{rup}}\right)$, and the other at $t = f\left(\frac{-\Delta\xi}{V_{rup}}\right)$, which would be zero since that point is ahead of the rupture front and has not been ruptured. The slip rate shape function, no matter what the shape is, would both start and end with a small value. Therefore, as long as $f\left(\frac{\Delta\xi}{V_{rup}}\right)$ is not near the peak value, $f\left(\frac{\Delta\xi}{V_{rup}}\right)$ would always likely be small, and thus $s(\xi^j, t^0)$ would be small as well. Additionally, based on Equation 9, if $\frac{\Delta\xi}{V_{rup}}$ is greater than the rise time T, $s(\xi^j, t^0)$ would strictly equal zero. Thus, the back-projection beam power does not correlate with the slip motion on the homogeneous rupture case.

Qualitatively, our synthetic results in the homogeneous model (Model A1) can be understood easily if we look at the source model in a different frame of reference: if the rupture front propagates at a constant velocity, we will always be able to find an inertial frame of reference that moves along with the rupture front. Furthermore, if all the rupture parameters are spatially homogeneous, the slip pulse at the rupture front will be static when viewed in the new co-moving inertial frame of reference, and thus will not radiate seismic energy. If the rupture does not radiate seismic energy in one inertial frame of reference, it does not radiate seismic energy in any inertial frame

of reference, including the frame at rest we originally used. We also refer to previous theoretical and numerical studies of the case of an infinitely propagating steady slip pulse in which all the total strain energy change is dissipated within the source region, implying no net radiated energy (Gabriel et al., 2012; Rice et al., 2005).

If we approximate $\Delta\xi$ as the P wave wavelength and V_{rup} as S wave velocity, assuming P wave is ~1.5 times larger than S wave, $\frac{\Delta\xi}{V_{rup}}$ could be approximated as ~1.5 times the period of a P wave seismogram. For Model A1 in which all rupture properties are homogeneous, the seismogram periods are 0.5–1 s (1–2 Hz) and the corresponding $\frac{\Delta\xi}{V_{rup}}$ would be ~0.75–1.5 s, which is about the same length as the slip rate shape duration (1 s). In this case, both $f\left(\frac{\Delta\xi}{V_{rup}}\right)$ and $f\left(\frac{-\Delta\xi}{V_{rup}}\right)$ would have a small value and thus $s(\xi^j, t^0)$ would be small. It explains why the beam power for the Model A1 rupture is low. This analysis could possibly explain why our theoretical relation between frequency and heterogeneity wavelength does not perfectly match the 3–5 Hz experiments (Section 4.2, Figures 3a3 and 3b3). At 3–5 Hz, $\frac{\Delta\xi}{V_{rup}}$ would be about 0.3–0.5 s, which is relatively small compared to the slip rate shape duration (1 s). In that case, the heterogeneity wavelength may not need to be as short as what Equation 8 predicts to cause significant beam power in a 3–5 Hz back-projection analysis. A comprehensive analysis of the slip rate shape and duration effect is needed to fully explain this issue, but will be subject to a future study.

5.2.3. Implications for Interpreting Back-Projection Beam Power

The above derivation suggests that, even though back-projection beam power is related to the spatial average of slip acceleration near the rupture front, as suggested by previous studies, it is not a good measure of the peak absolute slip acceleration amplitude near the rupture front. The key to generating a large beam power is not to have a large peak absolute slip acceleration; instead, the key is to have rupture heterogeneities that can mitigate the "cancellation effect", in the integral of Equation 10, which indicates that there is an intrinsic destructive interference of the wavefield governing the rupture front radiation.

There should be multiple ways to diminish the "cancellation effect" in the integral of Equation 10. Figure 8 shows schematic diagrams that demonstrate the spatial averaging effect of slip acceleration near the rupture front for Models A1-A4. For Model A1 where both the Green's function amplitude and all the rupture properties are homogeneous (Figure 8a), the positive slip acceleration contribution largely compensates for the slip deceleration contribution, leading to small beam power. However, if any of the rupture properties (Figures 8b and 8c) is heterogeneous, the positive and negative slip acceleration contributions do not cancel out, leading to large radiation. In Model A4, heterogeneity of local strike causes the radiation pattern factor to vary along the fault, which leads to a spatially heterogeneous Green's function amplitude (Figure 8d), which causes large beam power. We note that while we are using a symmetric slip rate function in the cartoon figures in Figure 8, rupture models with asymmetric slip rate functions, in principle, should give similar qualitative results. This is because the spatial integration of acceleration and deceleration near the rupture front, no matter what the shape is, always tends to be minimized because the slip rate will eventually go back to zero (complete stop) or close to zero (a trailing edge with low slip rate). A numerical evaluation of the asymmetric slip rate function would be interesting, but is outside the scope of discussion here.

Although simple, our proposed "cancellation effect" explanation is consistent with our synthetic back-projection results (Figure 2). Additionally, this explanation also suggests that any type of heterogeneity, not restricted to what we here explore, can cause high-frequency seismic radiation, as long as this heterogeneity can diminish the intrinsic destructive interference of the wavefield.

5.3. Physical Explanation for the Frequency- and Array-Dependent Back-Projection Results

Our synthetic experiments show that back-projection results for the same earthquake can be different when arrays are in different azimuths or seismograms are filtered in different frequency bands (Models A5, B, and C). Such frequency- and array-dependent results are also commonly observed for natural earthquakes, such as the 2019 New Ireland Earthquake as we demonstrate in Section 4.3, and many others (e.g., Kiser & Ishii, 2011; Kiser & Ishii, 2017; Koper et al., 2011; Lay et al., 2012; Yao et al., 2013). In subduction zones, short-period or higher frequency back-projection results often track the rupture on the downdip section of the subduction fault, and the ruptures on the updip fault are captured by lower frequency back-projection results. Some subduction slab models propose that in the seismogenic zone, which hosts large damaging earthquakes, the fault plane is characterized by asperities of different sizes (e.g., Galvez et al., 2014; Lay et al., 2012), which decreases in size with

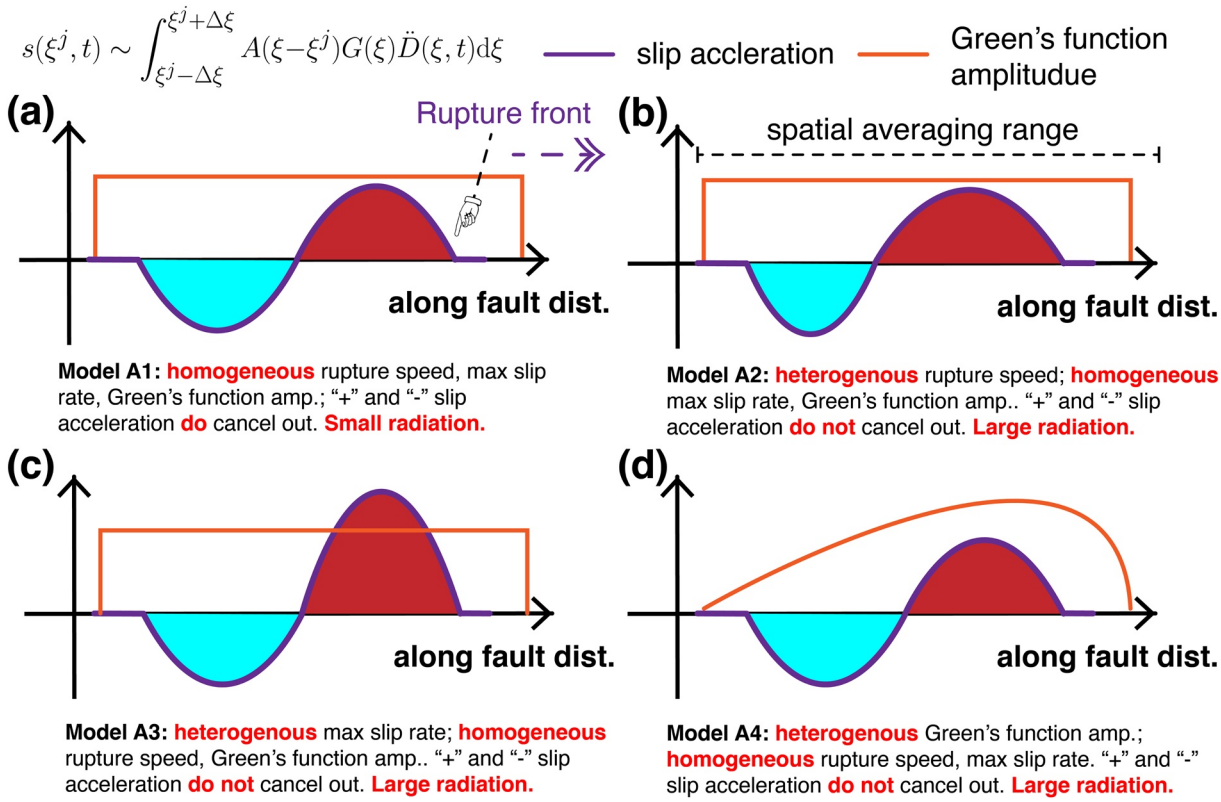

Figure 8. Schematic diagrams demonstrating the spatial averaging effect of slip acceleration near the rupture front. (a) In Model A1, where all the rupture properties are homogeneous, the positive lobe tends to cancel out the negative lobe, leading to small radiation. (b) In Model A2, where the rupture velocity is heterogeneous, the positive lobe could be longer than the negative lobe and thus cannot be canceled out, leading to large radiation. (c) In Model A3, where the maximum slip rate is heterogeneous, the positive lobe could be higher than the negative lobe and thus cannot be canceled out, leading to large radiation. (d) In Model A4, where the Green's function amplitude is heterogeneous, even though the positive lobe has an area that equals the negative lobe, the weights of these two lobes are different so they cannot cancel out, leading to large radiation.

increasing depth. During a large earthquake, asperities with a broad size range - from very large to small – are broken. Our theoretical analysis in Section 4 suggests that back-projection tends to capture the rupture whose heterogeneity wavelength matches the corresponding seismogram frequency, and the corresponding seismogram frequency is affected by both the wavelength spectrum of the rupture heterogeneity and rupture directivity. Some advancements have been proposed in back-projection to image complex ruptures with multiple sources in one time window (e.g., Wang et al., 2016; Yao et al., 2012). However, due to the source-array configuration, attenuation, heterogeneous velocity structures, localized noise and other factors that affect the data quality and coherence, some rupture branches could still be "hidden" in one array and result in frequency- and array-dependent rupture results.

Our analytical analysis of the high frequency radiation and back-projection beam power in Sections 5.1 and 5.2 can help explain the frequency- and array-dependent back-projection results observed in our study. In the "moment rate" analysis in Section 5.1, the high-frequency radiation is generated by the fluctuation of the moment rate function in time, and each period of the fluctuation corresponds to one wavelength of heterogeneity (Figures 7b and 7c). Therefore, a larger/shorter heterogeneity wavelength corresponds to a longer/shorter corresponding seismogram period. Since the total duration of the far-field pulse is modulated by the directivity effect (e.g., Shearer, 2019), the relationship between heterogeneity wavelength and seismogram frequency would also be modulated by the directivity effect.

In Section 5.2, we demonstrate that for a given array configuration and a chosen seismogram frequency range, back-projection beam power at the rupture front represents a weighted spatial average of slip acceleration. The weighted averaging calculation is affected by multiple factors such as the Green's function amplitude, maximum slip rate amplitude, and rupture propagation velocity (Equation 12). Most importantly, the area of the averaging

calculation has a dimension of $\Delta\xi$, which is the range where source signals can stack coherently and related to the size of ARF (Rost & Thomas, 2002). Since $\Delta\xi$ is frequency- and array-dependent, the back-projection results would be frequency- and array-dependent as well.

The above two approaches, though superficially different, have the same theoretical basis. The seismic wavefield at a propagating rupture front tends to feature destructive interference between adjacent points on the fault; thus, the fundamental condition to generate significant high-frequency radiation is to have spatial heterogeneities that can diminish the intrinsic destructive interference. The spatial characteristic of source heterogeneities is preserved in the shape of the wavefield. As the wavefield reaches the seismic stations, this spatial information of the wavefield will be "mapped" into the time information in the seismograms. The above two approaches are just two different ways to derive this "mapping" relation.

5.4. Simplifications and Limitations of Our Synthetic Experiments

All synthetic experiments in this study are simplified to allow the isolation of specific effects. Here we note several crucial simplifications and assumptions, justifying them and explaining their associated limitations for interpretation.

5.4.1. One-Dimensional Rupture on a Line Fault

The earthquake source in our models are all 1D ruptures on a line fault (Figure 1c). We neglect 2D rupture propagation effects, such as a curvature of the rupture front and mixed in-plane (mode II) and anti-plane (mode III) propagation (e.g., Madariaga et al., 1998). However, one-fault 1D models (Figures 1c1 and 1c2) are useful proxies to model rupture on an elongated fault (such as a long strike-slip rupture across a vertical fault, Weng and Ampuero (2019)). The two-fault 1D models can be considered as a crude analog of shallow and deeper ruptures that propagate simultaneously in a large megathrust earthquake, shedding light on how depth-dependent rupture properties may be resolved using back-projection.

5.4.2. Heterogeneity With a Sinusoidal Variation

The spatial variations of rupture parameters in all models are sinusoidal with a single wavelength. Since our main goal is only to investigate seismic radiation mechanisms rather than to model real earthquakes, sinusoidal variation is a natural way to theoretically relate heterogeneity wavelength (length scale) with seismogram frequency. A deeper rationale behind the choice of sinusoidal functions is that they are the basis functions for Fourier analysis. Inspired by the isochron theory of Spudich and Frazer (1984) and Bernard and Madariaga (1984), the velocity seismogram amplitude $\dot{u}(x,t)$ can be expressed in a general form as:

$$\dot{u}(x,t) \sim h(y(x,t)) = h(y), \tag{15}$$

in which y is the isochron location on the fault that corresponds to the observation point x and the observation time t. $h(y)$ is a complicated function that depends on the rupture properties and Green's function at location y. Therefore, when taking a Fourier transform on the left-hand side of Equation 15, the right-hand side can be re-organized as a function of heterogeneity wavelength λ:

$$\begin{aligned} U(f) &\approx \int_{t_1}^{t_2} \dot{u}(t)\exp(-i2\pi f t)\mathrm{d}t \\ &\approx \int_{t_1}^{t_2} h(y)\exp\left(-i2\pi f \frac{\partial \tau_a}{\partial y} y\right) \frac{\partial \tau_a}{\partial y}\mathrm{d}y + C \\ &= \int_{t_1}^{t_2} \left[h(y)\frac{\partial \tau_a}{\partial y}\right] \exp\left(-i2\pi \frac{1}{\lambda} y\right) \mathrm{d}y + C \\ &\approx R\left(\frac{1}{\lambda}\right) + C, \end{aligned} \tag{16}$$

in which $[t_1, t_2]$ is the time range of the P phase. Function $\tau_a(x, y)$ is the inverse of $y(x, t)$, which is the arrival time at observer x of a P wave emitted by point y when it ruptures. $R\left(\frac{1}{\lambda}\right)$ is the Fourier Transform of $h(y)\frac{\partial \tau_a}{\partial y}$ in space, and $\lambda = 1/\left(f\frac{\partial \tau_a}{\partial y}\right)$ is the wavelength. C is a constant in the integration.

The above derivation involves many simplifications and is non-rigorous. We speculate that a rigorous derivation of such a relation is possible (but beyond the scope of this study). Such a one-to-one relation between the

frequency component and wavelength component would enable us to easily extend our analysis to an arbitrarily heterogeneous rupture that has a complex wavelength spectrum.

5.4.3. Kinematic Models Instead of Dynamic Rupture Models

All our source models are kinematic rupture models in which fault slip and rupture evolution are pre-determined. The representation theorem relates moment tensor seismic sources with the seismic wavefield in the framework of elasto-dynamics (Aki & Richards, 2002). It implies that if we know the Green's function, seismic radiation can be fully represented by the convolution of the gradients of the Green's function with an arbitrary distribution of moment tensor body force equivalents of the spatial-temporal distribution of fault slip. Therefore, kinematic models make it easy and fast to separate the contributions of different kinematic parameters on the seismic radiation.

Dynamic rupture models that reproduce the physical processes that govern the way faults yield and slide combine spontaneous frictional failure and seismic wave propagation at a higher computational cost. In such highly non-linear models, different kinematic parameters are found to correlate (Schmedes et al., 2010). For example, rupture propagation velocity and maximum slip rate are both controlled largely by local shear stress, and these two parameters could well be tightly coupled (e.g., Day, 1982; Gabriel et al., 2013). Also, when there is a change in fault strike, it is likely that the rupture propagation velocity will experience a change as well (e.g., Oglesby & Mai, 2012). Similarly, small-scale fault roughness leads to high-frequency radiation (Shi & Day, 2013) and can be linked to two effects that arise due to the fault's non-planarity: variations in the out-of-plane position of local moment rate functions, and perturbations in moment tensor orientation (Mai et al., 2018). In the scope of investigating radiation mechanisms, using kinematic models may be sufficient, and indeed preferable, to tease apart separate effects; yet, we note that it is necessary to consider dynamic effects in order to make a model more similar to natural earthquake ruptures. We expect that the relation of the resultant non-linearly correlated kinematic quantities and far-field beam power will be similar to the current kinematic analysis, although it will be difficult to determine whether heterogeneity in slip rate is more important than heterogeneity in fault strike, for example, in any given earthquake that includes both effects.

5.4.4. Pulse-Like Rupture

In our synthetic experiments, ruptures are described as propagating pulses, and the pulse width in time is fixed as 1 s. Many numerical studies have suggested earthquake rupture may be crack-like (e.g., Gabriel et al., 2012; Lambert et al., 2021; Zheng & Rice, 1998), in which case the slip rate behind the rupture front can stay at high level for a longer time, and thus cause a wider high-slip-rate zone evolving behind the rupture front. The effects of such longer rise times are not explored here, but we note that the destructive interference factor exists in crack-like models as well. In addition, dynamic models with crack-like features also suggest that a change in rupture velocity would generate high-frequency radiation (e.g., Madariaga, 1983).

5.4.5. Far-Field P Waves Calculated With Full-Space Green's Function

In this study, we use a full-space elasto-dynamic analytical Green's function to compute the far-field P wave seismogram. Other phases that could potentially contaminate the P phase pulse, such as the depth phases (e.g., pP and sP), are not considered in our study. Additionally, wave propagation in this model suffers no attenuation. Our synthetic seismograms contain no noise, and the travel-time used in the back-projection analysis is exactly the same as the travel-time in the forward model. These conditions ensure that the back-projection on the synthetic seismograms can achieve perfect coherence, which is impossible in a real-world application. If one considers realistic path effects caused by heterogeneous 3D Earth media and noise, the synthetic seismograms will be less coherent and involve coda waves. Such synthetics with realistic waveform complexities can lead to both imaging artifacts and mislocation of high-frequency radiation sources (e.g., Bao & Meng, 2020; Zeng et al., 2020). However, we argue that it is reasonable to make the path effect as simple as possible, because we focus on the intrinsic source effects in this study. Our conclusions should be able to be applicable to more realistic cases with complicated velocity structures, as long as they are well constrained.

5.5. Implications

It is worth noting that in our synthetic experiments, the back-projection beam power is an array-based average representation of the far-field velocity waveforms. Thus our conclusions about the back-projection results, like

the effect of rupture heterogeneity and directivity, can be also applied to other methods that utilize the far-field waveforms at frequency higher than the earthquake corner frequency.

Although the models are simplified, our main conclusions are general enough to inform the interpretation of back-projection results for earthquakes, of which the rupture process can be successfully imaged. Depending on the data availability, data quality and coherence, rupture complexity and many other factors, it is impossible to determine what would be the minimum magnitude earthquake the back-projection and our analysis can be applied. Yin and Denolle (2019) constructed an empirical relation between resolvable area/earthquake magnitude and seismic frequencies, showing lower magnitude events need higher frequency to be resolved by back-projection. So far, back-projection has been successfully applied to image the rupture process of many moderate and large earthquakes, implying our framework would be applicable to most events above magnitude 6. Given appropriate data coverage and quality, our theoretical and dimension-independent framework should also hold for the analysis of smaller magnitude events.

5.5.1. Physical Significance of the Back-Projection Beam Power

Perhaps inspired by the success of finite-fault kinematic models, there is an expectation that the back-projection beam power could be directly related to certain physical characteristics of earthquake rupture, particularly near the rupture front, since beam power spatiotemporal variability is often found to correlate with the rupture propagation process. For example, if beam power is related to the peak slip acceleration amplitude at the rupture front (e.g., Fukahata et al., 2014; Okuwaki et al., 2019; Yao et al., 2012), it could be used to infer the mechanical parameters at the rupture front, since peak slip acceleration is directly related to the frictional properties at the rupture front, such as dynamic stress drop.

However, our results show that such a direct relation between beam power and the peak slip acceleration at the rupture front may not exist. We note that beam power rather should be related to a spatial average of slip acceleration near the rupture front, and is weighted by the Green's function. Since the positive slip acceleration and negative slip acceleration tend to cancel out near the rupture front, beam power from a point on the fault is not a good measure for the peak slip acceleration at that point. Instead, the main controlling factor of beam power is the extent of mitigation of destructive interference at the rupture front, caused primarily by heterogeneity in the seismic source. We find that the imbalance between slip acceleration and deceleration contributions can be caused by many different types of spatial heterogeneities on the fault, such as rupture velocity, maximum slip rate, or Green's function amplitude. Additionally, whether beam power can be significant depends on whether the heterogeneity wavelength matches the seismogram frequency, and this can also be modulated by rupture directivity. The slip rate can only be resolved in an ideal scenario when there is no noise contamination, all other types of spatial properties are homogeneous, and the slip rate is the only variation parameter. In addition, the variation wavelength needs to be much longer than the rupture process resolvability of back-projection, which is affected by the source-array configuration and length of the sliding time window. Then the spatial average of the slip rate acceleration near the rupture front will be proportional to the back-projection beam power performed with unfiltered waveforms. Such an idealized setup and results are illustrated in Figure S9 in Supporting Information S1.

5.5.2. A New Framework to Interpret Frequency- and Array-Dependent Results

We propose a simple theoretical framework, in terms of heterogeneity wavelength and rupture directivity, to systematically interpret the frequency- and array-dependent back-projection results for a single earthquake. When multiple rupture fronts propagate simultaneously, back-projection tends to capture the rupture branches whose radiation frequency matches the seismogram filtering range, and the radiation frequency is controlled by both heterogeneity wavelength and rupture directivity (causing “red-shifts” and “blue-shifts” in Figure 6c). The relation between radiation frequency and rupture heterogeneity wavelength is described in Equation 8. Although similar ideas have been suggested in many previous studies (e.g., Lay et al., 2012), such a quantitative framework hasn't been established before to the best of our knowledge.

We argue that this framework, although derived from simple models, should be applicable for complex earthquake ruptures as well. We have shown that this framework can not only be applied to successfully explain frequency and azimuth-dependent back-projection results in our synthetic experiments (Section 4.2), but also to interpret the 2019 New Ireland Earthquake, using both the linear back-projection method and the MUSIC back-projection method (Section 4.3, Figure S4 in Supporting Information S1). Therefore, we argue that this

novel theoretical framework should be widely applicable to extract useful information from natural earthquakes. More observations in the future can help to further test its robustness and applicability.

5.5.3. Revealing the Limitations of Sub-Event Analysis

Strong sources of high frequency energy from a large earthquake can dominate back-projection results for a few time windows, leading to rupture "clusters" on several patches in back-projection results. This effect sometimes is inferred to be sub-events that correspond to the breaking of multiple individual faults or fault patches. The beam power amplitude in each back-projection "cluster" is thought to be proportional to the sub-event's magnitude (e.g., Yao et al., 2012; Zeng et al., 2020). In the sub-event reference frame, the radiation appears as low-frequency, since it is of longer period than the sub-event's source dimension; however, this radiation would be treated as high-frequency radiation in the main event analysis.

Our study shows there are other explanations for an apparent sub-event separation observed in back-projection results, such as non-planar fault surfaces with various scales of frictional and geometrical asperities, or a heterogeneity the rupture encounters in its propagation, both of which are intrinsically different from self-contained sub-events on an individual subfault. Similar results have been reported in other theoretical results as well (e.g., Adda-Bedia & Madariaga, 2008; Dunham et al., 2011). For example, the seismic radiation generated by a kink on a fault is different from that of a double-couple moment tensor source (Adda-Bedia & Madariaga, 2008); however, this "kink phase" can still generate high beam power in the back-projection result.

5.5.4. Point Source Interval in a Forward Model for Synthetic Back-Projection Experiments

When conducting synthetic kinematic models with a finite number of discrete point sources, the spacing of point sources must be sufficiently dense to ensure that the radiation in the studied frequencies is not affected by the discrete spacing. In all our numerical experiments, the spacing of discrete point sources is 50 m. Considering that our smallest rupture heterogeneity wavelength is 1.59 km, and the shortest seismic wave wavelength we use is (5.6 km/s)/(5 Hz) = 1.1 km, the grid spacing in our setup should be small enough to resolve high-frequency radiation generated by rupture heterogeneity.

Figure S5 in Supporting Information S1 displays the beam power for homogeneous rupture models with different point source spacings. As the spacing grows, the back-projection method begins to resolve the discrete point sources, and thus can track the rupture. Of course, in the case of wide source spacing, the rupture can no longer truly be considered "homogeneous", which explains why this low-resolution source produces significant beam power as an artifact. More precisely, a forward source model with spatial discretization ΔS may introduce an artificial spatial heterogeneity (manifest as discrete point sources) with a characteristic wavelength of ΔS, which can produce ground motion in a related frequency range at an array. If this signal is within the frequency band of the back-projection analysis, even a "homogeneous" model can generate significant beam power that is related to the strength of each individual point source, which may lead to an artificial result that slip, slip rate, or slip acceleration at a point apparently correlates with back-projection beam power.

6. Conclusions

Our synthetic experiments, although simplified, provide a clear correlation between variations in different rupture parameters, such as the rupture velocity, peak slip rate, and fault-local strike orientation, and the back-projection results. Insignificant beam power in the spatially and temporally homogeneous rupture suggests the amplitude of far-field high frequency radiation does not necessarily correlate with the amplitude of any single rupture parameter, like the slip or slip rate, at the back-projected fault location. Instead, the rupture front naturally tends to have the accelerating and decelerating portions of slip rate to cancel each other out. Thus, the high frequency energy radiation is more related to the spatial heterogeneity of various rupture parameters, including but not limited to the three rupture parameters investigated in our synthetic experiments, around the rupture front. In addition, we propose that the heterogeneity of Green's function amplitude, which may be caused by fault geometry heterogeneity or medium heterogeneity, can also contribute to the high frequency signal at the array stations. Back-projection is able to image the rupture process of heterogeneous faults, but the beam power signatures of heterogeneity in different fault properties are not easily distinguishable from each other. Thus, back-projection alone may be unable to distinguish which type or types of source heterogeneity are responsible for the signal. It is also worth noting that our analysis is not limited to the back-projection technique, and can be extended to other

methods that utilize the properties of the far-field waves (e.g., Haskell, 1964; Spudich & Frazer, 1984), such as finite-fault inversions, which are characterized by non-unique solutions using the observed (seismic) data (e.g., Zhang et al., 2015; Mai et al., 2016; Ye et al., 2016).

We find that rupture heterogeneity and directivity combine to produce frequency- and array-dependent back-projection results. Based on the Doppler effect, we derive a quantitative relation between the heterogeneity wavelength and the dominant frequency of seismic recordings at the array. The theoretical relation demonstrates that a shorter/longer characteristic wavelength of the rupture heterogeneity radiates higher/lower frequency energy, and the "toward"/"backwards" array rupture changes the spectrum on the array recordings to a higher/lower frequency band, resulting in the back-projection being sensitive to a different frequency range of the source. For a complex rupture event with two or more simultaneous rupture fronts/branches, the back-projection tends to capture the rupture in a direction or on a branch that produces higher amplitude signals in the filtered frequency ranges by the array. This relation quantitatively explains the back-projection results in our synthetic experiments, as well as the array- and frequency-dependent results for the 2019 M7.6 bilateral-rupture New Ireland earthquake. Our study, even with its simplifications and limitations, can provide some guidelines to physically interpret back-projection results, especially for complex rupture events.

Data Availability Statement

The authors used the following networks and acknowledge them as follows: AK: Alaska Earthquake Center, Univ. of Alaska Fairbanks (1987). Alaska Regional Network [Data set]. International Federation of Digital Seismograph Networks. https://doi.org/10.7914/SN/AK. AT: NOAA National Oceanic and Atmospheric Administration (USA) (1967). National Tsunami Warning Center Alaska Seismic Network [Data set]. International Federation of Digital Seismograph Networks. https://doi.org/10.7914/SN/AT. AV: Alaska Volcano Observatory/USGS (1988). Alaska Volcano Observatory [Data set]. International Federation of Digital Seismograph Networks. https://doi.org/10.7914/SN/AV. BW: Department of Earth And Environmental Sciences, Geophysical Observatory, University of Munchen (2001). BayernNetz [Data set]. International Federation of Digital Seismograph Networks. https://doi.org/10.7914/SN/BW. CC: Cascades Volcano Observatory/USGS (2001). Cascade Chain Volcano Monitoring [Data set]. International Federation of Digital Seismograph Networks. https://doi.org/10.7914/SN/CC. CI: California Institute of Technology and United States Geological Survey Pasadena (1926). Southern California Seismic Network [Data set]. International Federation of Digital Seismograph Networks. https://doi.org/10.7914/SN/CI. CN: Natural Resources Canada (NRCAN Canada) (1975). Canadian National Seismograph Network [Data set]. International Federation of Digital Seismograph Networks. https://doi.org/10.7914/SN/CN. II: Scripps Institution Of Oceanography (1986). IRIS/IDA Seismic Network. International Federation of Digital Seismograph Networks. https://doi.org/10.7914/SN/II. IU: Albuquerque Seismological Laboratory (ASL)/USGS (1988). Global Seismograph Network (GSN—IRIS/USGS). International Federation of Digital Seismograph Networks. https://doi.org/10.7914/SN/IU. TA: IRIS Transportable Array (2003). USArray Transportable Array. International Federation of Digital Seismograph Networks. https://doi.org/10.7914/SN/TA. UW: University of Washington (1963). Pacific Northwest Seismic Network - University of Washington [Data set]. International Federation of Digital Seismograph Networks. https://doi.org/10.7914/SN/UW. Chinese array data is available upon request.

Acknowledgments
We thank Wenyuan Fan for sharing his preliminary results and providing us crucial advice and encouragement at the early stage of this study. We thank Yongfei Wang for the insightful discussion on the isochron theory of seismic radiation and its implication on the back-projection analysis. We thank Gareth Funning, James Dieterich, Guanshui Xu, Junlin Hua, Ryo Okuwaki, Han Yue, Zengxi Ge, and Chao Song for evaluating our preliminary results and providing suggestions on the project scope and experimental design. We also want to extend our thanks to the editor Yehuda Ben-Zion, the anonymous associate editor, Jiuxun Yin and other two anonymous reviewers for their constructive comments that greatly improved the content of this manuscript. Figures are plotted using Generic Mapping Tools (http://gmt.soest.hawaii.edu) and Matlab. B. Li and A.-A. Gabriel acknowledge funding from the European Research Council (ERC) under the European Union's Horizon 2020 research and innovation programme (ChEESE, Grant Nos. 823844 and TEAR, Grant No. 852992), by the German Research Foundation (DFG; grants no. GA 2465/2-1, GA 2465/3-1), the National Science Foundation (NSF Grant No. EAR-2121666), and by KAUST-CRG (Grant No. ORS-2017-CRG6 3389.02). Abhijit Ghosh is supported by NSF EAR-1620655 and 1358686. H. Bao and L. Meng are supported by NSF EAR-1848486 and by Leon and Joann V.C. Knopoff Fund. Open access funding enabled and organized by Projekt DEAL.

References

Adda-Bedia, M., & Madariaga, R. (2008). Seismic radiation from a kink on an antiplane fault. *Bulletin of the Seismological Society of America*, *98*(5), 2291–2302.

Aki, K., & Richards, P. G. (2002). *Quantitative seismology*.

Ammon, C. J., Velasco, A. A., Lay, T., & Wallace, T. C. (2020). *Foundations of modern global seismology*. Academic Press.

Bao, H., Ampuero, J.-P., Meng, L., Fielding, E. J., Liang, C., Milliner, C. W., & Huang, H. (2019). Early and persistent supershear rupture of the 2018 magnitude 7.5 Palu earthquake. *Nature Geoscience*, *12*(3), 200–205.

Bao, H., & Meng, L. (2020). Quantifying the mislocation of back-projection imaging due to velocity heterogeneities beneath the source region. *AGU Fall Meeting Abstracts*, *2020*, 0433–02.

Bernard, P., & Madariaga, R. (1984). A new asymptotic method for the modeling of near-field accelerograms. *Bulletin of the Seismological Society of America*, *74*(2), 539–557.

Bouchon, M., & Vallée, M. (2003). Observation of long supershear rupture during the magnitude 8.1 Kunlunshan earthquake. *Science*, *301*(5634), 824–826.

Chen, K., Milliner, C., & Avouac, J.-P. (2019). The Weitin Fault, Papua New Guinea, ruptured twice by mw 8.0 and mw 7.7 earthquakes in 2000 and 2019. *Geophysical Research Letters*, *46*(22), 12833–12840.

Crotwell, H. P., Owens, T. J., & Ritsema, J. (1999). The TauP Toolkit: Flexible seismic travel-time and ray-path utilities. *Seismological Research Letters*, *70*(2), 154–160.

Day, S. M. (1982). Three-dimensional simulation of spontaneous rupture: The effect of nonuniform prestress. *Bulletin of the Seismological Society of America*, *72*(6A), 1881–1902.

Dunham, E. M., & Archuleta, R. J. (2004). Evidence for a supershear transient during the 2002 Denali fault earthquake. *Bulletin of the Seismological Society of America*, *94*(6B), S256–S268.

Dunham, E. M., Belanger, D., Cong, L., & Kozdon, J. E. (2011). Earthquake ruptures with strongly rate-weakening friction and off-fault plasticity, part 2: Nonplanar faults. *Bulletin of the Seismological Society of America*, *101*(5), 2308–2322.

Fan, W., & Shearer, P. M. (2015). Detailed rupture imaging of the 25 April 2015 Nepal earthquake using teleseismic p waves. *Geophysical Research Letters*, *42*(14), 5744–5752.

Fan, W., & Shearer, P. M. (2017). Investigation of backprojection uncertainties with m6 earthquakes. *Journal of Geophysical Research: Solid Earth*, *122*(10), 7966–7986.

Fukahata, Y., Yagi, Y., & Rivera, L. (2014). Theoretical relationship between back-projection imaging and classical linear inverse solutions. *Geophysical Journal International*, *196*(1), 552–559.

Gabriel, A.-A., Ampuero, J.-P., Dalguer, L., & Mai, P. M. (2013). Source properties of dynamic rupture pulses with off-fault plasticity. *Journal of Geophysical Research: Solid Earth*, *118*(8), 4117–4126.

Gabriel, A.-A., Ampuero, J.-P., Dalguer, L. A., & Mai, P. M. (2012). The transition of dynamic rupture styles in elastic media under velocity-weakening friction. *Journal of Geophysical Research: Solid Earth*, *117*(B9).

Galetzka, J., Melgar, D., Genrich, J. F., Geng, J., Owen, S., & Lindsey, E. O. (2015). Slip pulse and resonance of the Kathmandu basin during the 2015 Gorkha earthquake, Nepal. *Science*, *349*(6252), 1091–1095.

Gallovič, F., Valentová, L., Ampuero, J.-P., & Gabriel, A.-A. (2019). Bayesian dynamic finite-fault inversion: 2. Application to the 2016 mw 6.2 Amatrice, Italy, earthquake. *Journal of Geophysical Research: Solid Earth*, *124*(7), 6970–6988.

Galvez, P., Ampuero, J.-P., Dalguer, L. A., Somala, S. N., & Nissen-Meyer, T. (2014). Dynamic earthquake rupture modelled with an unstructured 3-d spectral element method applied to the 2011 m 9 Tohoku earthquake. *Geophysical Journal International*, *198*(2), 1222–1240.

Gothard, L. Q., & Rosen, J. (2010). *Encyclopedia of physical science (facts on file science library) (volume 1 & 2)*. Facts on File.

Hamling, I. J., Hreinsdóttir, S., Clark, K., Elliott, J., Liang, C., & Fielding, E. (2017). Complex multifault rupture during the 2016 mw 7.8 Kaikōura earthquake, New Zealand. *Science*, *356*(6334).

Hartzell, S. H., & Heaton, T. H. (1983). Inversion of strong ground motion and teleseismic waveform data for the fault rupture history of the 1979 Imperial Valley, California, earthquake. *Bulletin of the Seismological Society of America*, *73*(6A), 1553–1583.

Haskell, N. (1964). Total energy and energy spectral density of elastic wave radiation from propagating faults. *Bulletin of the Seismological Society of America*, *54*(6A), 1811–1841.

Hayes, G. P., Briggs, R. W., Sladen, A., Fielding, E. J., Prentice, C., & Hudnut, K. (2010). Complex rupture during the 12 January 2010 Haiti earthquake. *Nature Geoscience*, *3*(11), 800–805.

Ishii, M., Shearer, P. M., Houston, H., & Vidale, J. E. (2005). Extent, duration and speed of the 2004 Sumatra-Andaman earthquake imaged by the hi-net array. *Nature*, *435*(7044), 933–936.

Kiser, E., & Ishii, M. (2011). The 2010 mw 8.8 Chile earthquake: Triggering on multiple segments and frequency-dependent rupture behavior. *Geophysical Research Letters*, *38*(7).

Kiser, E., & Ishii, M. (2017). Back-projection imaging of earthquakes. *Annual Review of Earth and Planetary Sciences*, *45*, 271–299.

Koper, K. D., Hutko, A. R., Lay, T., Ammon, C. J., & Kanamori, H. (2011). Frequency-dependent rupture process of the 2011 m w 9.0 Tohoku earthquake: Comparison of short-period p wave backprojection images and broadband seismic rupture models. *Earth Planets and Space*, *63*(7), 599–602.

Krüger, F., & Ohrnberger, M. (2005). Tracking the rupture of the m w = 9.3 Sumatra earthquake over 1,150 km at teleseismic distance. *Nature*, *435*(7044), 937–939.

Lambert, V., Lapusta, N., & Perry, S. (2021). Propagation of large earthquakes as self-healing pulses or mild cracks. *Nature*, *591*(7849), 252–258.

Lay, T., Ammon, C., Kanamori, H., Koper, K., Sufri, O., & Hutko, A. (2010). Teleseismic inversion for rupture process of the 27 February 2010 Chile (mw 8.8) earthquake. *Geophysical Research Letters*, *37*(13).

Lay, T., Kanamori, H., Ammon, C. J., Koper, K. D., Hutko, A. R., Ye, L., & Rushing, T. M. (2012). Depth-varying rupture properties of subduction zone megathrust faults. *Journal of Geophysical Research: Solid Earth*, *117*(B4).

Li, B. (2019). *A broad spectrum of fault behaviors in fast and slow earthquakes*. University of California.

Li, B., & Ghosh, A. (2017). Imaging rupture process of the 2015 mw 8.3 Illapel earthquake using the US seismic array. In *The Chile-2015 (Illapel) earthquake and tsunami* (pp. 33–43). Springer.

Lindley, I. D.(2006). In G. Lavecchia, & G. Scalera (Eds.), *Extensional and vertical tectonics in the New Guinea islands: Implications for island arc evolution* (pp. 403–426).

Liu, P., Archuleta, R. J., & Hartzell, S. H. (2006). Prediction of broadband ground-motion time histories: Hybrid low/high-frequency method with correlated random source parameters. *Bulletin of the Seismological Society of America*, *96*(6), 2118–2130.

Madariaga, R. (1977). High-frequency radiation from crack (stress drop) models of earthquake faulting. *Geophysical Journal International*, *51*(3), 625–651.

Madariaga, R. (1978). The dynamic field of Haskell's rectangular dislocation fault model. *Bulletin of the Seismological Society of America*, *68*(4), 869–887.

Madariaga, R. (1983). High frequency radiation from dynamic earthquake. *Annals of Geophysics*, *1*, 17.

Madariaga, R., Ampuero, J.-P., & Adda-Bedia, M. (2006). *Seismic radiation from simple models of earthquakes*.

Madariaga, R., Olsen, K., & Archuleta, R. (1998). Modeling dynamic rupture in a 3d earthquake fault model. *Bulletin of the Seismological Society of America*, *88*(5), 1182–1197.

Mai, P. M., Galis, M., Thingbaijam, K. K., Vyas, J. C., & Dunham, E. M. (2018). Accounting for fault roughness in pseudo-dynamic ground-motion simulations. In *Best practices in physics-based fault rupture models for seismic hazard assessment of nuclear installations* (pp. 95–126). Springer.

Mai, P. M., Schorlemmer, D., Page, M., Ampuero, J.-P., Asano, K., & Causse, M. (2016). The earthquake-source inversion validation (siv) project. *Seismological Research Letters*, *87*(3), 690–708.

Meier, M.-A., Ampuero, J., & Heaton, T. H. (2017). The hidden simplicity of subduction megathrust earthquakes. *Science*, *357*(6357), 1277–1281.

Meng, L., Ampuero, J.-P., Sladen, A., & Rendon, H. (2012). High-resolution backprojection at regional distance: Application to the Haiti m7. 0 earthquake and comparisons with finite source studies. *Journal of Geophysical Research: Solid Earth*, *117*(B4).

Meng, L., Bao, H., Huang, H., Zhang, A., Bloore, A., & Liu, Z. (2018). Double pincer movement: Encircling rupture splitting during the 2015 mw 8.3 Illapel earthquake. *Earth and Planetary Science Letters*, *495*, 164–173.

Meng, L., Inbal, A., & Ampuero, J.-P. (2011). A window into the complexity of the dynamic rupture of the 2011 mw 9 Tohoku-oki earthquake. *Geophysical Research Letters*, *38*(7).

Meng, L., Zhang, A., & Yagi, Y. (2016). Improving back projection imaging with a novel physics-based aftershock calibration approach: A case study of the 2015 Gorkha earthquake. *Geophysical Research Letters*, *43*(2), 628–636.

Mikumo, T., & Miyatake, T. (1993). Dynamic rupture processes on a dipping fault, and estimates of stress drop and strength excess from the results of waveform inversion. *Geophysical Journal International*, *112*(3), 481–496.

Oglesby, D. D., & Mai, P. M. (2012). Fault geometry, rupture dynamics and ground motion from potential earthquakes on the north Anatolian fault under the Sea of Marmara. *Geophysical Journal International*, *188*(3), 1071–1087.

Okuwaki, R., Kasahara, A., Yagi, Y., Hirano, S., & Fukahata, Y. (2019). Backprojection to image slip. *Geophysical Journal International*, *216*(3), 1529–1537.

Rice, J. R., Sammis, C. G., & Parsons, R. (2005). Off-fault secondary failure induced by a dynamic slip pulse. *Bulletin of the Seismological Society of America*, *95*(1), 109–134.

Ross, Z. E., Idini, B., Jia, Z., Stephenson, O. L., Zhong, M., & Wang, X. (2019). Hierarchical interlocked orthogonal faulting in the 2019 Ridgecrest earthquake sequence. *Science*, *366*(6463), 346–351.

Rost, S., & Thomas, C. (2002). Array seismology: Methods and applications. *Reviews of Geophysics*, *40*(3), 2–1.

Schmedes, J., Archuleta, R. J., & Lavallée, D. (2010). Correlation of earthquake source parameters inferred from dynamic rupture simulations. *Journal of Geophysical Research: Solid Earth*, *115*(B3).

Shearer, P. M. (2019). *Introduction to seismology*. Cambridge university press.

Shi, Z., & Day, S. M. (2013). Rupture dynamics and ground motion from 3-d rough-fault simulations. *Journal of Geophysical Research: Solid Earth*, *118*(3), 1122–1141.

Sieh, K., Jones, L., Hauksson, E., Hudnut, K., Eberhart-Phillips, D., & Heaton, T. (1993). Near-field investigations of the landers earthquake sequence, april to july 1992. *Science*, *260*(5105), 171–176.

Spudich, P., & Frazer, L. N. (1984). Use of ray theory to calculate high-frequency radiation from earthquake sources having spatially variable rupture velocity and stress drop. *Bulletin of the Seismological Society of America*, *74*(6), 2061–2082.

Tan, F., Ge, Z., Kao, H., & Nissen, E. (2019). Validation of the 3-d phase-weighted relative back projection technique and its application to the 2016 m w 7.8 Kaikōura earthquake. *Geophysical Journal International*, *217*(1), 375–388.

Tinti, E., Fukuyama, E., Piatanesi, A., & Cocco, M. (2005). A kinematic source-time function compatible with earthquake dynamics. *Bulletin of the Seismological Society of America*, *95*(4), 1211–1223.

Toksoz, M., Reilinger, R., Doll, C., Barka, A., & Yalcin, N. (1999). Izmir (Turkey) earthquake of 17 august 1999: First report. *Seismological Research Letters*, *70*(6), 669–679.

Tregoning, P., Jackson, R. J., McQueen, H., Lambeck, K., Stevens, C., Little, R. P., & Rosa, R. (1999). Motion of the south Bismarck plate, Papua New Guinea. *Geophysical Research Letters*, *26*(23), 3517–3520.

Vallée, M., Charléty, J., Ferreira, A. M., Delouis, B., & Vergoz, J. (2011). SCARE: A new technique for the rapid determination of seismic moment magnitude, focal mechanism and source time functions for large earthquakes using body-wave deconvolution. *Geophysical Journal International*, *184*(1), 338–358.

Wang, D., Takeuchi, N., Kawakatsu, H., & Mori, J. (2016). Estimating high frequency energy radiation of large earthquakes by image deconvolution back-projection. *Earth and Planetary Science Letters*, *449*, 155–163.

Weng, H., & Ampuero, J.-P. (2019). The dynamics of elongated earthquake ruptures. *Journal of Geophysical Research: Solid Earth*, *124*(8), 8584–8610.

Xu, Y., Koper, K. D., Sufri, O., Zhu, L., & Hutko, A. R. (2009). Rupture imaging of the mw 7.9 12 May 2008 Wenchuan earthquake from back projection of teleseismic p waves. *Geochemistry, Geophysics, Geosystems*, *10*(4).

Yagi, Y., Nakao, A., & Kasahara, A. (2012). Smooth and rapid slip near the Japan trench during the 2011 Tohoku-oki earthquake revealed by a hybrid back-projection method. *Earth and Planetary Science Letters*, *355*, 94–101.

Yagi, Y., & Okuwaki, R. (2015). Integrated seismic source model of the 2015 Gorkha, Nepal, earthquake. *Geophysical Research Letters*, *42*(15), 6229–6235.

Yao, H., Gerstoft, P., Shearer, P. M., & Mecklenbräuker, C. (2011). Compressive sensing of the Tohoku-oki mw 9.0 earthquake: Frequency-dependent rupture modes. *Geophysical Research Letters*, *38*(20).

Yao, H., Shearer, P. M., & Gerstoft, P. (2012). Subevent location and rupture imaging using iterative backprojection for the 2011 Tohoku m w 9.0 earthquake. *Geophysical Journal International*, *190*(2), 1152–1168.

Yao, H., Shearer, P. M., & Gerstoft, P. (2013). Compressive sensing of frequency-dependent seismic radiation from subduction zone megathrust ruptures. *Proceedings of the National Academy of Sciences*, *110*(12), 4512–4517.

Ye, L., Lay, T., Kanamori, H., & Rivera, L. (2016). Rupture characteristics of major and great (mw 7.0) megathrust earthquakes from 1990 to 2015: 1. Source parameter scaling relationships. *Journal of Geophysical Research: Solid Earth*, *121*(2), 826–844.

Yin, J., & Denolle, M. A. (2019). Relating teleseismic backprojection images to earthquake kinematics. *Geophysical Journal International*, *217*(2), 729–747.

Yin, J., Yang, H., Yao, H., & Weng, H. (2016). Coseismic radiation and stress drop during the 2015 mw 8.3 Illapel, Chile megathrust earthquake. *Geophysical Research Letters*, *43*(4), 1520–1528.

Zeng, H., Wei, S., & Wu, W. (2020). Sources of uncertainties and artefacts in back-projection results. *Geophysical Journal International*, *220*(2), 876–891.

Zhang, H., & Ge, Z. (2010). Tracking the rupture of the 2008 Wenchuan earthquake by using the relative back-projection method. *Bulletin of the Seismological Society of America*, *100*(5B), 2551–2560.

Zhang, H., Van Der Lee, S., & Ge, Z. (2016). Multiarray rupture imaging of the devastating 2015 Gorkha, Nepal, earthquake sequence. *Geophysical Research Letters*, *43*(2), 584–591.

Zhang, L., Mai, P. M., Thingbaijam, K. K., Razafindrakoto, H. N., & Genton, M. G. (2015). Analysing earthquake slip models with the spatial prediction comparison test. *Geophysical Journal International*, *200*(1), 185–198.

Zheng, G., & Rice, J. R. (1998). Conditions under which velocity-weakening friction allows a self-healing versus a cracklike mode of rupture. *Bulletin of the Seismological Society of America*, *88*(6), 1466–1483.